Oxidative Damages on the Alzheimer's Related-Aβ Peptide Alters Its Ability to Assemble

Clémence Cheignon, Fabrice Collin, Laurent Sabater, Christelle Hureau

antioxidants

MDPI

Article

Oxidative Damages on the Alzheimer's Related-Aβ Peptide Alters Its Ability to Assemble

Clémence Cheignon †, Fabrice Collin ‡, Laurent Sabater and Christelle Hureau *

LCC-CNRS, Université de Toulouse, CNRS, 31077 Toulouse, France
* Correspondence: christelle.hureau@lcc-toulouse.fr
† Current addresses: Equipe de Synthèse Pour l'Analyse, SynPAUniversité de Strasbourg, CNRS, IPHC UMR 7178, 67037 Strasbourg, France.
‡ Current addresses: UMR 5623 IMRCP, CNRS, 31000 Toulouse, France.

Abstract: Oxidative stress that can lead to oxidation of the amyloid-β (Aβ) peptide is considered a key feature in Alzheimer's disease (AD), influencing the ability of Aβ to assemble into β-sheet rich fibrils that are commonly found in senile plaques of AD patients. The present study aims at investigating the fallouts of Aβ oxidation on the assembly properties of the Aβ peptide. To accomplish this, we performed kinetics and analysis on an oxidized Aβ (^{ox}Aβ) peptide, resulting from the attack of reactive oxygen species (ROS) that are formed by the biologically relevant Cu/Aβ/dioxygen/ascorbate system. ^{ox}Aβ was still able to assemble but displayed ill-defined and small oligomeric assemblies compared to the long and thick β-sheet rich fibrils from the non-oxidized counterpart. In addition, ^{ox}Aβ does affect the assembly of the parent Aβ peptide. In a mixture of the two peptides, ^{ox}Aβ has a mainly kinetic effect on the assembly of the Aβ peptide and was able to slow down the formation of Aβ fibril in a wide pH range [6.0–7.4]. However, ^{ox}Aβ does not change the quantity and morphology of the Aβ fibrils formed to a significant extent. In the presence of copper or zinc di-cations, ^{ox}Aβ assembled into weakly-structured aggregates rather than short, untangled Cu-Aβ fibrils and long untangled Zn-Aβ fibrils. The delaying effect of ^{ox}Aβ on metal altered Aβ assembly was also observed. Hence, our results obtained here bring new insights regarding the tight interconnection between (i) ROS production leading to Aβ oxidation and (ii) Aβ assembly, in particular via the modulation of the Aβ assembly by ^{ox}Aβ. It is the first time that co-assembly of ^{ox}Aβ and Aβ under various environmental conditions (pH, metal ions . . .) are reported.

Keywords: oxidative stress; peptide; assembly; copper; zinc

Citation: Cheignon, C.; Collin, F.; Sabater, L.; Hureau, C. Oxidative Damages on the Alzheimer's Related-Aβ Peptide Alters Its Ability to Assemble. *Antioxidants* **2023**, *12*, 472. https://doi.org/10.3390/antiox12020472

Academic Editor: Anna Colell

Received: 28 December 2022
Revised: 27 January 2023
Accepted: 7 February 2023
Published: 13 February 2023

1. Introduction

Alzheimer's disease (AD) is one of the most, if not the most, well-known amyloid-related diseases. Amyloids refer to a specific arrangement of very stable, intrinsically disordered peptides by the alignment of β-sheets perpendicular to the longer axis [1–3]. Given this, amyloid deposits are found in a large panel of pathologies, such as AD, Type-II diabetes Mellitus, Parkinson's disease and systemic amyloidosis [4,5]. In AD, the senile plaques made of the extracellular deposits of Amyloid-β (Aβ) peptides in the fibrillar state (*id est*, as amyloids) is the first pathological hallmark of the disorder [6–8], whilst the second one is the intraneuronal neurofibrillary tangles made of hyperphosphorylated Tau protein [9–11].

The assembly processes leading to the formation of amyloids are extremely complex, featuring many steps and species at play [2,3,12]. A simplified view is given in Scheme 1, wherein the formation of fibrils is highlighted and pathways leading to the formation of less-structured or amorphous species are also illustrated. It is worth noting that the in vitro assays on amyloid proteins are thoroughly described in the literature as mirrors of the in vivo assembly processes, and that in vitro investigations of assembly

represent a powerful tool to better understand in vivo assembly and are a crucial step to understand the biological mechanisms involved [13,14]. The self-assembly occurs through nucleation/elongation/secondary nucleation paths [12,14–18]. Nucleation is the formation of high-energy and low-molecular weight soluble intermediates from the monomers, wherein several kinds of intermediates can co-exist. Among them, metastable partially folded oligomers and nuclei can further elongate at their extremities. On the other hand, there are secondary nucleation processes that make the self-assembly of peptides auto catalytic [14,15]. Two main pathways can co-exist. The former is independent of the monomers concentration and corresponds to fragmentation of the fibrils, leading to shorter fibrils that can further elongate; the latter consists of fibrils-catalyzed nucleation, depending on the monomers concentration, and induces the formation of new nuclei by interaction of the monomers with the surface of the fibrils [19]. Furthermore, the self-assembly of amyloid-forming peptides depends on several parameters. The main parameter is the sequence of the peptide itself, but environmental factors, such as pH, can also affect these processes [20]. In the case of the Aβ peptides, the cleavage from the Amyloid Protein Precursor (APP) by β- and γ-secretases is heterogeneous, thus generating peptides of different lengths (up to 42 amino-acids). $A\beta_{1–40}$ and $A\beta_{1–42}$, 40 and 42 amino-acid residues long peptides are the most studied ones in the context of AD. Both N-terminal modification and C-terminal truncation impact Aβ self-assembly ability. Beyond that, Aβ peptides of different lengths can co-assemble along several mechanisms [21–28]. Recently, we found that $A\beta_{4–40}$ and $A\beta_{1–40}$ co-assemble faster than either peptide self-assembles independently [21]. Other examples include the co-assembly of $A\beta_{1/11–40}$ with $A\beta_{1–42}$, that proceeds as two independent self-assemblies [22,23], whilst $A\beta_{11–40}$ can recruit $A\beta_{1–40}$ in a process where $A\beta_{11–40}$ imposes its assembly properties [22] and $A\beta_{5–42}$ can seed the self-assembly of $A\beta_{1–42}$ [24]. More recently, the co-assembly of genetic Artic and Italian variants with $A\beta_{1–40/42}$ were also studied [25]. Hence, these various co-assembly processes need to be taken into account to mirror, as much as possible, the intrinsic biological complexity.

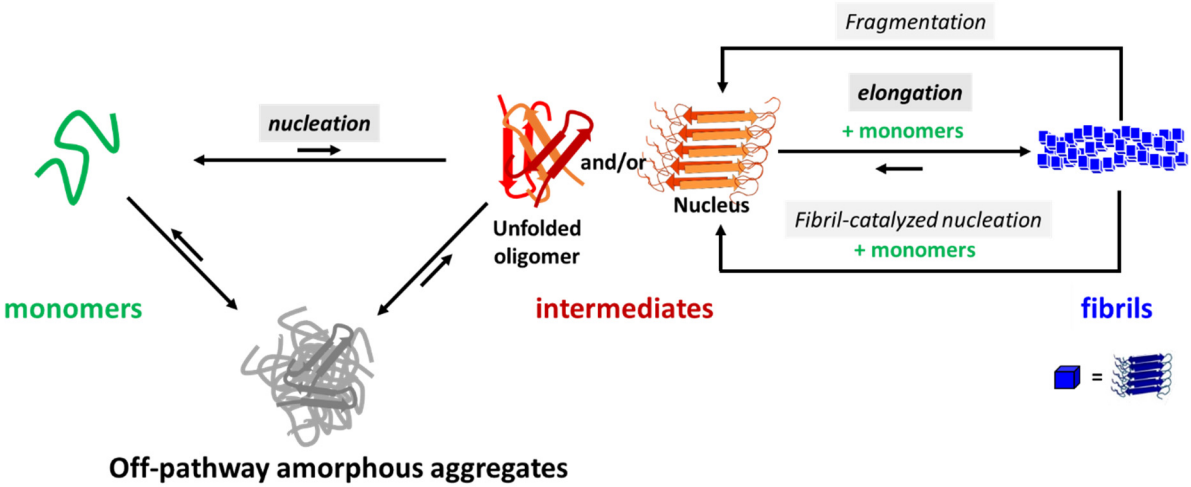

Scheme 1. Simplified scheme of the self-assembly of the $A\beta_{1–40}$ peptide showing nucleation, elongation and secondary nucleation steps, as well as off-pathways leading to amorphous aggregates. Elongation occurs from nuclei by the addition of monomers at their extremities. Secondary nucleation steps include the monomer-dependent fibril-catalyzed nucleation and monomer-independent fragmentation processes. Blue cubes in the fibrils correspond to the stacking of peptides under β-sheets.

Another key feature of AD is the post-mortem detection of oxidative damages, not only occurring on the biomolecules in the surroundings of the amyloid deposits, but also on the Aβ peptides themselves [29]. Indeed, the ability of the Aβ-bound Cu (Cu-Aβ) to generate reactive oxygen species (ROS) can contribute to the oxidative stress fallouts detected in AD patients. It is mainly due to the presence of an exchangeable pool of Cu (about 1–10 μM) [30] and ascorbate at a fairly high level (about 100–300 μM), in the

synaptic cleft [31–33], that can fuel the incomplete reduction of dioxygen to ROS, catalyzed by Cu-Aβ [29]. The Cu-Aβ-induced oxidative modifications of $A\beta_{1–40}$ described in the literature are illustrated in Scheme 2. Amino acid residues involved in Cu(I) and Cu(II) coordination [30] were found to be the main targets of ROS produced at the metal center: Asp1 oxidation and/or oxidative cleavage [34–37] and His13/His14 oxidation to oxo-histidine [34–41]). Phe19/20 [34,35,38] and Met35 [35,37,39] oxidations were also reported. Furthermore, tyrosine oxidation generating a dityrosine unit was only detected in a few studies [42–44]. This is probably because it is a minor oxidation, as reported recently [44,45], and/or due to the intrinsic detection challenge [45]. Other oxidative cleavages were also previously reported [36] at Ala2/Glu3, Val12/His13 and His13/His14 positions.

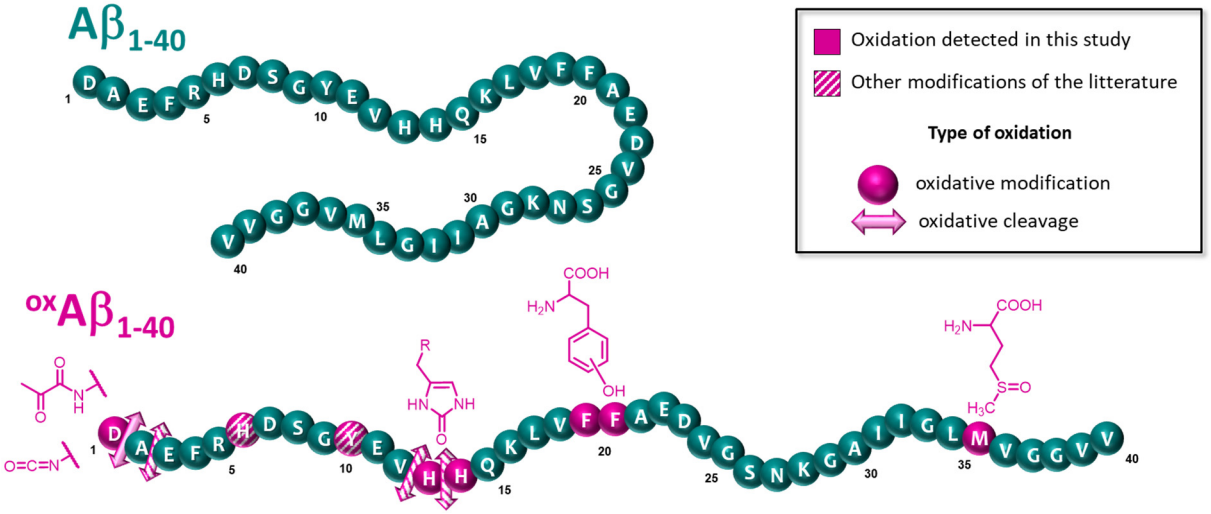

Scheme 2. Summary of Cu-$A\beta_{1–40}$-induced oxidative damages on $A\beta_{1–40}$ (damages using the ascorbate/O_2 oxidizing system are illustrated in pink and those found in other oxidative conditions, such as the use of H_2O_2, are illustrated in hatched pink).

In addition to the redox-active Cu ions, Zn(II) was found at 10–100 µM in the synaptic cleft. Both ions were detected in the amyloid plaques at millimolar level and were described as modulators of Aβ self-assembly in vitro, leading to Aβ assemblies of different morphologies, which led to various neurotoxic effects. Despite no strong consensus on the in vitro data, several points of convergence [30,46–48] support that (i) the effects of Cu(II) and Zn(II) on Aβ assembly are metal-dependent and metal-peptide ratio dependent and (ii) at the sub-molar level (versus $A\beta_{1–40}$), Cu(II) and Zn(II) mainly impact kinetics of amyloid formation and delay the assembly process, whilst at 1:1 stoichiometric and higher ratio, Cu(II) and Zn(II) impact the morphologies of the assemblies formed. Cu(II) favors shorter and thinner amyloids, while Zn(II) fosters ill-defined and amorphous aggregates.

Additionally, iron impairment is another contributor to AD pathology, which was found in senile plaques [49,50]. However, its exact role is not fully understood [50,51] and its speciation is not clear, with nanoparticles of mainly Fe, such as magnetite or ferritin-based minerals, being detected in the core of the plaques [49]. In contrast to Cu and Zn for which the molecular interaction with Aβ was characterized, only a few studies proposed a possible coordination site for the Fe(II)-Aβ [52] or Fe(III)-Aβ complex [53]. Despite the fact that the Fe(II)/Fe(III) redox couple may participate to the oxidative stress linked to AD [54,55], there is no evidence that this may be due to the Fe(II)/Fe(III)-Aβ interaction. There is also no study on the Fe(II) impact on the Aβ self-assembly, even if rare findings in this context were obtained for Fe(III) [56–59] or ferritin nanoparticles [60]. Therefore, the present report is focused on the impact of the metal ions Cu(II) and Zn(II) on the assembly of Aβ.

A relationship between the self-assembly of $A\beta_{1–40}$ and Cu-Aβ-induced ROS production ability was previously shown. On the one hand, it has been reported that Cu-$A\beta_{1–40}$ intermediate-size assemblies and fibrils produce less ROS than the Cu-$A\beta_{1–40}$ monomer, a propensity that is shared by α-synuclein, another amyloid-forming peptide involved in Parkinson's disease [61,62]. On the other hand, the mechanisms leading to site-specific oxidation of Aβ that affect its assembly propensity were only investigated in a few studies, mainly in non-physiological conditions, such as cold atmospheric plasma-induced oxidation [63] and hydroxyl radical-based fast photochemical oxidation [64], or focused on one specific amino acid residue oxidation, such as Met35 oxidation by hydrogen peroxide [65–68] and tyrosine oxidation, leading to dimer formation [43,44,69]. Dityrosine cross-links were shown to impede fibril formation and form soluble aggregates and/or short fibrils in the presence of copper [43,44,69]. Conversely, the effect of oxidized Met35 in $A\beta_{1–40}$ peptide is less clear. Several trends were reported: slower assembly but no effect on the morphology of the aggregates [65], shorter lag-time of fibril formation [67,68] along with the promotion of fragmented fibrils [67] and a lessening of oligomers formation [66].

In addition to those studies where oxidation at one specific amino-acid residues were explored, our main focus was to study (i) whether and to what extent the biologically relevant combination of oxidized peptides (noted $^{ox}A\beta_{1–40}$) [31,34,35,70,71], formed by the Cu-Aβ/ascorbate/dioxygen triad [35], self-assembles and modulates the assembly of $A\beta_{1–40}$ and (ii) the difference in the metal-modulated assembly of $^{ox}A\beta_{1–40}$ compared to $A\beta_{1–40}$ peptides. Given this, this work contributes to delineate the impact of physiologically relevant oxidative damages on the assembly of Aβ peptide to close the loop between Cu-Aβ ROS production and Aβ assembly, the two most important molecular and supra-molecular events related to the etiology of AD.

In the present article, we report on the self-assembly of $^{ox}A\beta_{1–40}$, $A\beta_{1–40}$ and a mixture of them in various ratios, at several pH, and compare Cu and Zn-modulated aggregation of $A\beta_{1–40}$ and $^{ox}A\beta_{1–40}$ using kinetics and imaging experiments, whilst the detailed analysis of $^{ox}A\beta_{1–40}$ formation was previously reported [35]. Such fundamental and basic research is fully required [72] to fully understand the molecular interactions responsible for Aβ assembly, wherein the close relationship between oxidative stress and Aβ self-assembly may play a major role in AD pathology [29,73,74].

2. Materials and Methods

2.1. Chemicals

A total of 0.1 M stock solutions of Cu(II) and Zn(II) (from $CuSO_4.5(H_2O)$ and $ZnSO_4(H_2O)$, respectively, purchased from Sigma (St. Louis, MO, USA)) were prepared in ultrapure water. Phosphate buffer was bought from Sigma-Aldrich (St. Louis, MO, USA) and dissolved in ultrapure water to reach a 0.1 M concentration. Bioluminescence grade HEPES buffer (sodium salt of 2-[4-(2-hydroxyethyl)piperazin-1-yl]ethanesulfonic acid) was bought from Honeywell Fluka (Morristown, NJ, USA) and dissolved in ultrapure water to reach a 0.5 M concentration. Tris hydrochloride (Tris-HCl) was purchased from Fluka and dissolved in ultrapure water to reach 1 M concentration, and was adjusted with NaOH to pH 11.0. Guanidinium chloride >99% was bought from Alfa Aesar (Haverhill, MA, USA) and was freshly prepared by dissolving the powder in Tris-HCl 0.1 M to reach a 6 M concentration. A 5 mM ascorbate solution was freshly prepared a few minutes prior to each experimental set by dissolving sodium L-ascorbate (Sigma) in ultrapure water. Ethylene diamine tetraacetic acid (EDTA) was purchased from Sigma-Aldrich and dissolved in ultrapure water to reach a 40 mM concentration. A stock solution of Thioflavin T (ThT) at 250 µM was prepared in water without any further purification, with ThT bought from Acros Organics (Waltham, MA, USA).

2.2. Peptide Preparation

All the synthetic peptides were bought from GeneCust (Dudelange, Luxembourg), with purity grade > 95%. Stock solutions of the $A\beta_{1–40}$ (sequence DAEFRHDSGYEVHHQK-

LVFFAEDVGSNKGAIIGLMVGGVV) peptide were prepared by dissolving the powder (~3 mg) in 500 µL of Tris-HCl (0.1 M) with Guanidinium chloride (6 M). The solutions were incubated at 20 °C overnight and purified by Fast Protein Liquid Chromatography (FPLC) (column Superdex 75, elution solvent NaOH 15 mM with NaCl 150 mM, flow rate 0.5 mL/min). The peptide concentration in the recovered fractions (500 µL) was then determined by UV-visible absorption of Tyr10, considered as free tyrosine (at pH 12, $(\varepsilon_{293} - \varepsilon_{360})$ = 2400 M^{-1} cm^{-1}). The solution was used as soon as possible in ThT fluorescence experiments.

2.3. Peptide Oxidation

A stock solution of $A\beta_{1–40}$ peptide was made fresh by dissolving the powder in 15 mM NaOH and titrated by UV-visible absorption of Tyr10, considered as free tyrosine (at pH 12, $(\varepsilon_{293} - \varepsilon_{360})$ = 2400 M^{-1} cm^{-1}). The $A\beta_{40}$ peptide (60 µM) was oxidized in a phosphate buffered solution (50 mM, pH 7.4) containing Cu(II) (50 µM) and ascorbate (0.5 mM) for 30 min. Then, the solution was concentrated with an Amicon Ultra 3 kDa membrane (Millipore, Burlington, MA, USA), washed with EDTA (10 equivalents) to remove copper and then washed with water. The oxidized peptide solution was recovered, incubated at 20 °C overnight with Tris-HCl (0.1 M) with Guanidinium chloride (6 M) [pH 10] and purified by Fast Protein Liquid Chromatography (FPLC) (column Superdex 75, elution solvent NaOH 15 mM with NaCl 150 mM, flow rate 0.5 mL/min). The peptide concentration in the recovered fractions (500 µL) was then determined by UV-visible absorption of Tyr10, considered as free tyrosine (at pH 12, $(\varepsilon_{293} - \varepsilon_{360})$ = 2400 $M^{-1}cm^{-1}$). Since the oxidized peptide solution has a background absorbance at 293 nm, the curve is fitted to subtract the absorbance due to the tailing from the Tyr absorption, as previously described [70]. The solution was used as soon as possible in ThT fluorescence experiments.

2.4. ThT Assay for $A\beta_{1–40}$ and $^{ox}A\beta_{1–40}$ Aggregation

Fluorescence experiments were performed on a FLUOstar Optima microplate reader system (BMG Labtech, Ortenberg, Germany) at 37 °C. Thioflavin-T (ThT) was used as a probe for β-sheet structures' formation [75,76]. Fluorescence was measured every 5 min during about 120 to 160 h (depending on the experiment), after 15 s of shaking at 200 rpm. A total of 384-well microplates were used, with a total volume of 100 µL for each sample. The time course of ThT fluorescence was then measured (excitation at 440 ± 10 nm, emission at 490 ± 10 nm). For experiments in the presence of metal ions, Cu(II) or Zn(II) was added in the solution as the last reagent. All the conditions were not systematically performed on the 4 independent experiments (the quantity of peptide available for one experiment is limited).

2.5. Transmission Electron Microscopy (TEM)

Solutions were collected from the fluorescence microplate after 120 to 150 h and prepared for TEM using the conventional negative staining procedure. An amount of 20 µL of the solution was adsorbed on Formvar-carbon-coated grids for 2 min, blotted and negatively stained with uranyl acetate (1%) for 1 min. Grids were examined with a TEM (Jeol JEM-1400, JEOL Inc, Peabody, MA, USA) at 80 kV. Images were acquired using a digital camera (Gatan Orius, Gatan Inc, Pleasanton, CA, USA) at 10,000× or 25,000× magnification. Since the phosphate buffer reacts with uranyl acetate, HEPES buffer was preferred and employed for TEM experiments, and thus, for ThT fluorescence experiments as well.

2.6. Determination of the Percentage of Remaining Non-Oxidized Peptides in the Solution of $^{ox}A\beta_{1–40}$ Peptide

The remaining $A\beta_{1–40}$ was evaluated by HPLC/HR-MS (Dionex Ultimate 300O coupled to LTQ-Orbitrap, ThermoScientific, Waltham, MA, USA). A total of 5 µL of the control $A\beta_{1–40}$ (non-oxidized) and $^{ox}A\beta_{1–40}$ were injected onto the column (Acclaim 120 C18,

50 × 3 mm, 3 µm, ThermoScientific) at room temperature. The gradient elution was carried out with formic acid 0.1% (mobile phase A) and acetonitrile/water (80/20 *v*/*v*) formic acid 0.1% (mobile phase B), at a flow rate of 500 µL min^{-1}. The mobile phase gradient was programmed with the following time course: 5% mobile phase B at 0 min, held 3 min, linear increase to 55% B at 8 min, linear increase to 100% of B at 9 min, held 2 min, linear decrease to 5% B at 12 min and held 3 min. The mass spectrometer was used as a detector, working in the full scan positive mode between m/z 150 and 2000, at a resolution power of 60,000. Extracted chromatograms (accuracy 5 ppm) were obtained for the most intense ions of $A\beta_{1–40}$ in our experimental conditions, i.e., $[M+4H]^{4+}$ and $[M+5H]^{5+}$ (respectively detected at m/z 1082.7949 and m/z 866.4375). According to ref [35], chromatographic peaks were integrated, and the remaining $A\beta_{1–40}$ in $^{ox}A\beta_{1–40}$ samples was found to be in the 10–40% range, depending on the performed experiment, as illustrated in Supporting Information for experiment 1, for which 15 ± 3% of the remaining $A\beta_{1–40}$ was evaluated.

3. Results

3.1. Oxidative Damages Leading to $^{ox}A\beta_{1–40}$

The detailed and full kinetic analysis of the oxidative damages undergone by the $A\beta_{1–40}$ peptide have been previously reported [35]. Hence, the characterization of the oxidation of the $A\beta_{1–40}$ peptide is given in the Supporting Information (Figures S1 and S2). The results are fully consistent with those previously reported on another peptide batch [35], which is in line with the correct replicability of such a Cu-Aβ/ascorbate/dioxygen oxidation procedure [34].

3.2. Self-Assembly of $A\beta_{1–40}$ and $^{ox}A\beta_{1–40}$ and Their Co-Assembly

Figure 1 shows the fluorescence enhancement of the Thioflavin-T (ThT) dye upon assembly of $A\beta_{1–40}$ and $^{ox}A\beta_{1–40}$, and of a 1:1 stoichiometric mixture of them, for four independent experiments. ThT fluorescence is currently the golden standard to evaluate the formation of β-sheet rich supramolecular architectures, due to the strong enhancement of its fluorescence (by about a 10^4-fold) upon interaction with amyloids [77,78]. This is fully appropriate for the screening of various conditions on plate fluorimeters. Of important note, it is well described that having reproducible assembly data for amyloid-forming peptides, such as Aβ, is highly challenging [12,79], but this is a pre-requisite to efficiently discuss assembly trends, as well as the effects of the aggregation's modifiers. Given this, we report four independent studies (termed experiments N°1 to 4) on which the conditions were performed, at least in triplicates. For $A\beta_{1–40}$ and $^{ox}A\beta_{1–40}$, ThT fluorescent kinetic traces show the classical s-shape curves corresponding to the nucleation-elongation supramolecular polymerization process, as previously described (Scheme 1). Several mathematical models have been proposed to reproduce such curves, the simplest one being given in Equation (1), while others that are more sophisticated have been reported to consider the asymmetry of the curve or double-sigmoidal process [12,21,80,81].

$$F(t) = F_0 + \frac{F_{max} - F_0}{\left(1 + exp^{-k(t-t_{1/2})}\right)} \text{ and } t_{lag} = t_{1/2} - \frac{2}{k} \quad (1)$$

where F_0 is the starting ThT fluorescence value, F_{max} is the maximum of ThT intensity, $t_{1/2}$ is the time at which the ThT fluorescence equals $\frac{F_{max}+F_0}{2}$ and k is the elongation rate.

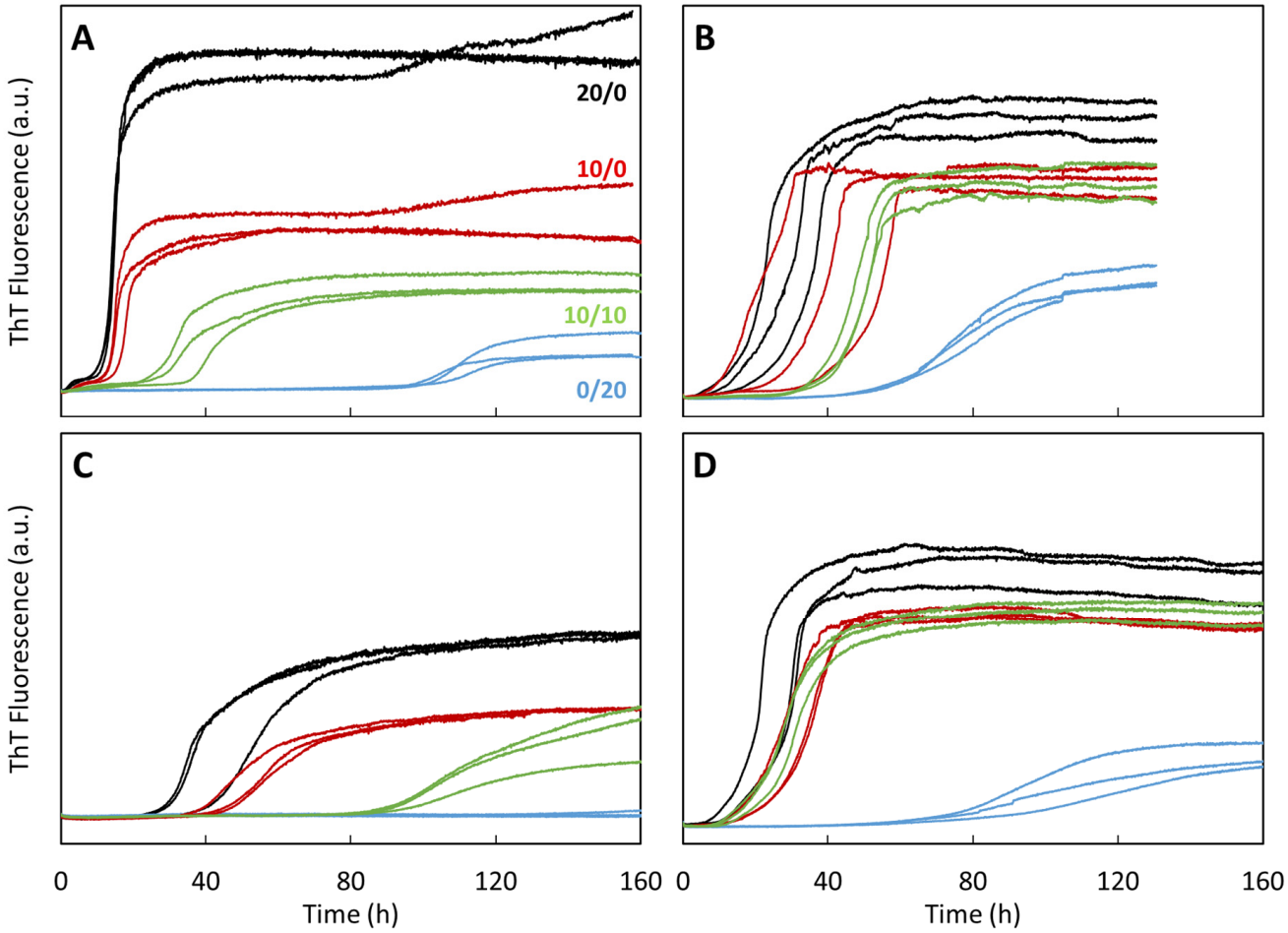

Figure 1. Kinetic monitoring of $A\beta_{1-40}$ and $^{ox}A\beta_{1-40}$ co-assembly using ThT fluorescence for 4 independent experiments. Curves are shown as triplicate. [$A\beta_{1-40}$] = 20 µM (black); [$^{ox}A\beta_{1-40}$] = 20 µM (blue); [$A\beta_{1-40}$] = [$^{ox}A\beta_{1-40}$] = 10 µM (green) and [$A\beta_{1-40}$] = 10 µM (red). Experiment N°1 (**A**), N°2 (**B**), N°3 (**C**) and N°4 (**D**). Hepes buffer 50 mM, [NaCl] = 65 mM, pH 7.0 (except 7.4 for experiment N°3). Y-axis corresponds to ThT fluorescence in arbitrary unit (a.u.); data are directly comparable between them (same y-scale).

We observed two main features (Figure 1): (i) $A\beta_{1-40}$ (black lines) and $^{ox}A\beta_{1-40}$ (blue lines) show very different self-assembly trends, with $A\beta_{1-40}$ having a decreased $t_{1/2}$ (2 to 10-fold) and much higher F_{max} values (2.5 to 4-fold) than $^{ox}A\beta_{1-40}$, consistently observed in the four independent experiments reported. However, the quantitative differences between $A\beta_{1-40}$ and $^{ox}A\beta_{1-40}$ vary from one experiment to another, hypothesized to be due to the level of remaining non-oxidized $A\beta_{1-40}$ in $^{ox}A\beta_{1-40}$ samples (about 10% in experiments 1 and 3 and about 30 and 40% in experiments 4 and 2, respectively; see Material and Methods for details); (ii) the comparison of assembly from a 1:1 stoichiometric mixture of $A\beta_{1-40}$ and $^{ox}A\beta_{1-40}$ (10 µM each, green lines), or from the control with $A\beta_{1-40}$ only (10 µM, red lines), shows that $^{ox}A\beta_{1-40}$ induces a slowdown of the $A\beta_{1-40}$ assembly that cannot be driven by dilution effect only. The extent of this effect is even more obvious in experiments 1 and 3 when compared to experiments 2 and 4. For the latter ones, the levels of $A\beta_{1-40}$ and $^{ox}A\beta_{1-40}$ are under- and over-estimated, respectively, since some non-oxidized $A\beta_{1-40}$ is present in $^{ox}A\beta_{1-40}$ samples. The higher real [$A\beta_{1-40}$] and lower real [$^{ox}A\beta_{1-40}$] (up to 13–15 µM and down to 5–7 µM in these two experiments) counterbalanced the slow down effect of $^{ox}A\beta_{1-40}$. In addition, the F_{max} values for both conditions ([$A\beta_{1-40}$] = 10 µM + [$^{ox}A\beta_{1-40}$] = 10 µM and [$A\beta_{1-40}$] = 10 µM) are similar, suggesting that,

despite the $^{ox}A\beta_{1-40}$ having a kinetic effect on $A\beta_{1-40}$ assembly, it is not recruited to form fibrils together with $A\beta_{1-40}$, which would have led to an increase in ThT fluorescence intensity.

Beyond kinetic differences in their formation mechanisms, the final species obtained from the assembly of $A\beta_{1-40}$ and $^{ox}A\beta_{1-40}$ show different morphologies. TEM pictures taken at the end of $A\beta_{1-40}$ assembly display long, mature fibrils ranging from 200 nm to 1 µm in length (Figure 2A). For $^{ox}A\beta_{1-40}$, several kinds of aggregates with different morphologies are observed, including mainly amorphous species, but also oligomers and shorter and thinner fibrils (Figure 2B). This is in line with the lower final fluorescence intensity of $^{ox}A\beta_{1-40}$ compared to $A\beta_{1-40}$. It is also worth noting that fibrils may come from the remaining unoxidized peptide in the $^{ox}A\beta_{1-40}$ sample. These results suggest that $^{ox}A\beta_{1-40}$ keeps the ability to self-assemble, but with lower propensity to form fibrils than $A\beta_{1-40}$, which is in line with the weaker ThT intensity. In the presence of both $^{ox}A\beta_{1-40}$ and $A\beta_{1-40}$, amorphous aggregates are found together with fibrils longer and thinner than those observed in the absence of $^{ox}A\beta_{1-40}$ (Figure 2D). This is not only a dilution effect since no ill-defined assemblies are observed when $[A\beta_{1-40}]$ = 10 µM (Figure 2C). Overall, TEM pictures indicate that $^{ox}A\beta_{1-40}$ and $A\beta_{1-40}$ may form independent assemblies, which is in line with the ThT kinetic data.

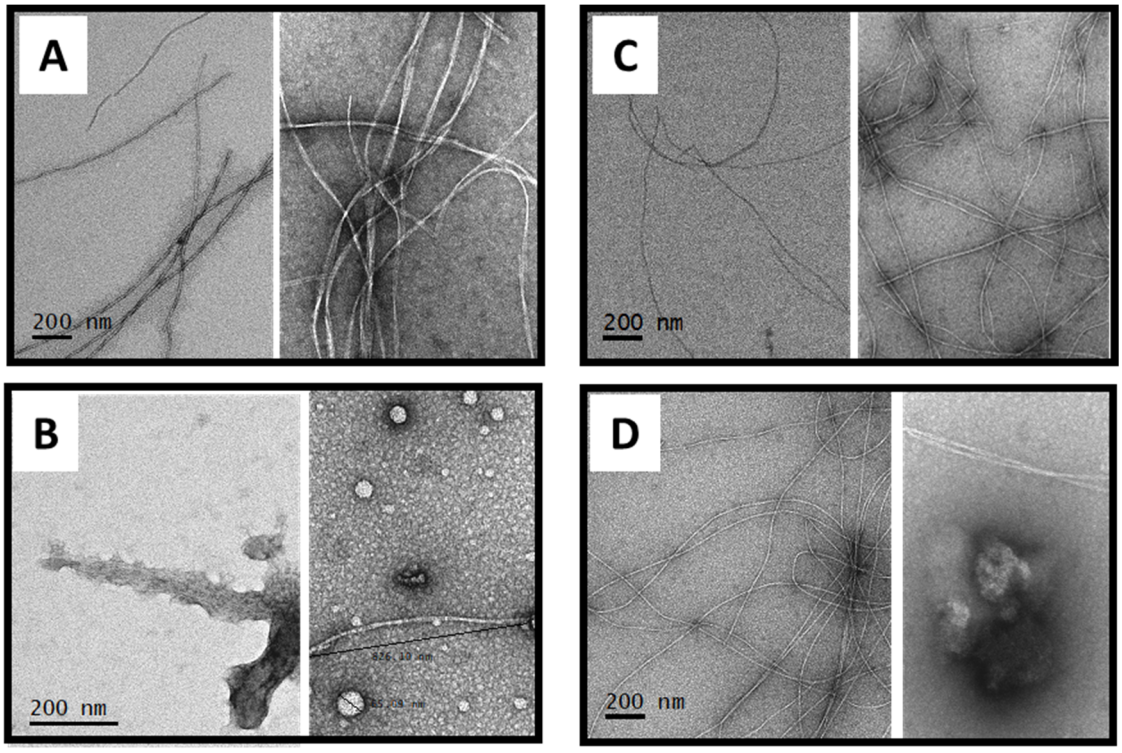

Figure 2. Representative TEM pictures of (**A**) 20 µM $A\beta_{1-40}$, (**B**) 20 µM $^{ox}A\beta_{1-40}$, (**C**) 10 µM $A\beta_{1-40}$ and (**D**) 10 µM $A\beta_{1-40}$ + 10 µM $^{ox}A\beta_{1-40}$ taken at the end of the ThT fluorescence experiment N°3. Hepes buffer 50 mM, [NaCl] = 65 mM, pH 7.4. Two shots are given to better illustrate the heterogeneity of the assemblies formed. The scale bar is the same for all shots in the same panel (200 nm).

3.3. Impact of pH on the Self-Assembly of $A\beta_{1-40}$ and $^{ox}A\beta_{1-40}$ and Their Co-Assembly

The effect of pH on the assembly of $A\beta_{1-40}$, $^{ox}A\beta_{1-40}$ and of a mixture at 1:1 stoichiometric ratio was investigated in experiment N°1 (Figure 3) and experiment N°3 (Figure S3). We found different pH-dependent effects on $A\beta_{1-40}$ and $^{ox}A\beta_{1-40}$ self-assembly. From $A\beta_{1-40}$ kinetics assessment, pH mainly modifies the shape of the s-curve, while $t_{1/2}$ and F_{max} values are almost unaffected (less than 20%). With respect to the shape of the curve, this result is in good agreement with a recent seminal and thorough study focusing on the origin of the pH-dependent assembly of $A\beta_{1-40}$ [20]. Concerning the $t_{1/2}$ value,

our results are in contrast with previously published work [20], which may be attributed to the four times higher concentration we used. From $^{ox}A\beta_{1-40}$ kinetics assessment and, conversely, to $A\beta_{1-40}$, the $t_{1/2}$ values of the $^{ox}A\beta_{1-40}$ self-assembly strongly depends on the pH, with an increase of $t_{1/2}$ observed as a function of pH. In addition, the delaying effect of $^{ox}A\beta_{1-40}$ on $A\beta_{1-40}$ assembly is kept with similar features as those described in the previous section, regardless of the pH values.

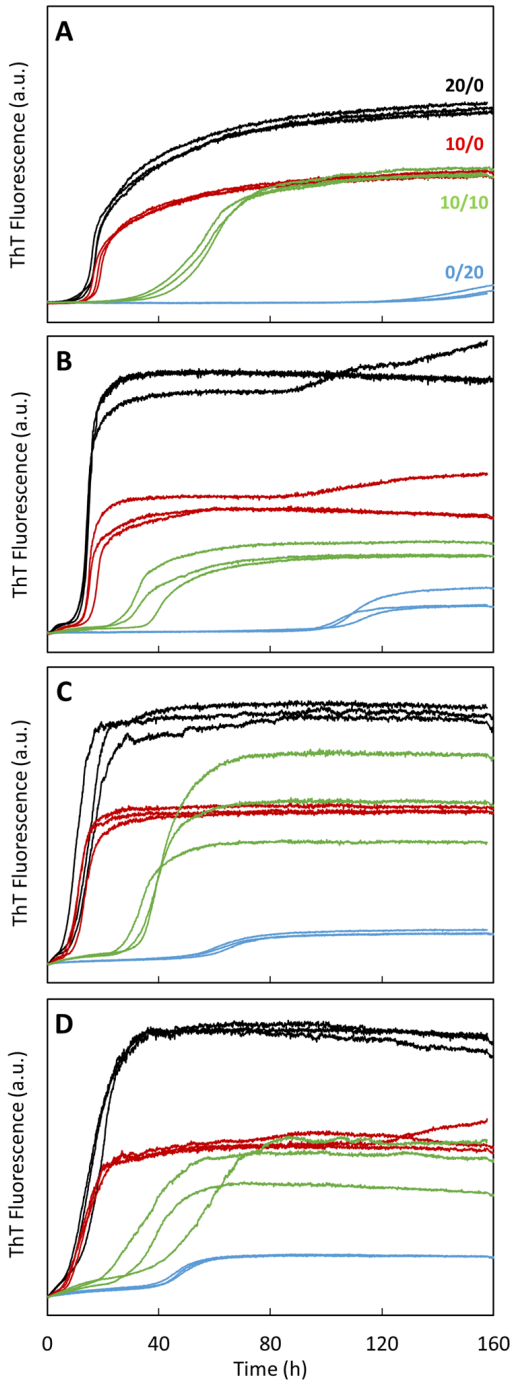

Figure 3. Kinetic monitoring of $A\beta_{1-40}$ and $^{ox}A\beta_{1-40}$ co-assembly using ThT fluorescence as a function of pH. Curves are shown as triplicate. $[A\beta_{1-40}]$ = 20 µM (black); $[^{ox}A\beta_{1-40}]$ = 20 µM (blue); $[A\beta_{1-40}] = [^{ox}A\beta_{1-40}]$ = 10 µM (green) and $[A\beta_{1-40}]$ = 10 µM (red). pH 7.4 (**A**), 7.0 (**B**), 6.5 (**C**) and 6.0 (**D**). From experiment N°1: Hepes buffer 50 mM, [NaCl] = 65 mM. Y-axis corresponds to ThT fluorescence in arbitrary unit (a.u.); data are directly comparable between them (same y-scale).

TEM pictures recorded at the end of the two self-assembly processes are shown in Figures S4 and S5 (experiments N°1 and 3, respectively). They show some differences in the assemblies of $A\beta_{1-40}$ and $^{ox}A\beta_{1-40}$ as a function of pH. We observed the formation of longer and twisted fibrils at a higher pH for $A\beta_{1-40}$ and more fibrillary assemblies at a lower pH for $^{ox}A\beta_{1-40}$, in line with the kinetics of assembly previously described in this work.

The kinetic effect of $^{ox}A\beta_{1-40}$ on $A\beta_{1-40}$ assembly, previously described at pH 7.0, is conserved regardless of the pH values (in the range of 6.0 to 7.4). In addition, as for $A\beta_{1-40}$, the pH has no or little effect on the assembly of the 1:1 stoichiometric mixture of $A\beta_{1-40}$ and $^{ox}A\beta_{1-40}$, followed by $t_{1/2}$ values falling in the same timescale (about 35 h). These results indicate that the strongly pH-dependent rate of $^{ox}A\beta_{1-40}$ assembly has little impact on the co-assembly process at these ratios and concentrations.

3.4. Co-Assembly of $A\beta_{1-40}$ and $^{ox}A\beta_{1-40}$ at Various Ratios and Concentrations

Further insights into the co-assembly of $A\beta_{1-40}$ and $^{ox}A\beta_{1-40}$ were provided by incubating the two peptides at various ratios, namely $[A\beta_{1-40}]/[^{ox}A\beta_{1-40}]$ = 20/0, 18/2, 16/4, 10/10, 4/16, 2/18 and 0/20 µM. The results obtained in experiment N°1 at 20/0, 16/4, 10/10, 4/16 and 0/20, along with 4/0, 10/0 and 16/0 for comparison, are shown in Figure 4A–C (see all data gathered in Figure S6 for experiments N°1 to 3), and the $t_{1/2}$ and F_{max} values, plotted as a function of the ratio between peptides, are shown in Figure 4D,E. At first glance, these data confirm our previous observations (described for the 1:1 stoichiometric ratio) for all the studied ratios, *id est*, the assembly slowed down with a higher $t_{1/2}$ in the presence of $^{ox}A\beta_{1-40}$, while F_{max} values mainly depended on the $A\beta_{1-40}$ concentration, regardless of the presence of $^{ox}A\beta_{1-40}$. A closer inspection of the $t_{1/2}$, as a function of $A\beta_{1-40}$ concentration, suggests a two-step trend: a significant decrease at low concentrations up to 10 µM, followed by a plateau between 10 and 20 µM. In the presence of $^{ox}A\beta_{1-40}$, the decrease of $t_{1/2}$ with increasing $A\beta_{1-40}$ concentration follows a more linear trend compared to $A\beta_{1-40}$ alone (red versus green dots in Figure 4D). Therefore, the slowdown, due to the presence of $^{ox}A\beta_{1-40}$, is more pronounced at $^{ox}A\beta_{1-40}/A\beta_{1-40}$ 1:1 stoichiometric ratio and above. At a lower $^{ox}A\beta_{1-40}/A\beta_{1-40}$ ratio, there is still a delaying effect, suggesting that $^{ox}A\beta_{1-40}$ acts on the first nucleation phase. However, the impact of $^{ox}A\beta_{1-40}$ on the slope of s-shape curves is not similarly observed between experiments. Despite an obvious weakening of the slope k, induced by $^{ox}A\beta_{1-40}$ in experiment N°1, this effect is not as clear for experiments N°2 and N°3 (Figure S6). Hence, this will not be commented on here.

Two other sets of experiments were additionally performed, wherein several concentrations of $A\beta_{1-40}$ were added to $^{ox}A\beta_{1-40}$ at 20 µM, and vice versa. The resulting kinetic ThT fluorescence data are shown in Figure 5A (experiment N°1), Figure S8 (experiments N°2 and 4) and Figure S9 (experiments N°1, 2 and 4), respectively. When $A\beta_{1-40}$ is added to $^{ox}A\beta_{1-40}$, the results are in line with previous observations (Figure 4), as an increased concentration of $A\beta_{1-40}$ is associated with an increase of F_{max} (Figure 5C) and a decrease of $t_{1/2}$ (Figure 5B) values. The concentration dependence of the kinetics of $A\beta_{1-40}$, in the presence of $^{ox}A\beta_{1-40}$ at 20 µM (Figure 5B), differs from that of $A\beta_{1-40}$ (in the absence of $^{ox}A\beta_{1-40}$ at 20 µM, Figure 4D). In addition, a higher positive slope of the co-assembly of $A\beta_{1-40}$ and $^{ox}A\beta_{1-40}$ curves relates to the amount of $A\beta_{1-40}$ added to the samples (Figure 5D). Note that here, k' has been calculated as the slope between $(t(F = F_{min} + \Delta F/0.8); F_{min} + \Delta F/0.8)$ and $(t(F = F_{min} + \Delta F/0.2); F_{min} + \Delta F/0.2)$. The comparison between $A\beta_{1-40}$ in the presence or absence of $^{ox}A\beta_{1-40}$ indicates that $^{ox}A\beta_{1-40}$ may play a dual role; a higher positive slope and increase in $t_{1/2}$, observed in $A\beta_{1-40}$ kinetics, supports an impact on both the nucleation and growth phases, whilst a similar trend is qualitatively observed for experiments N°2 and 4 (Figure S8).

When $^{ox}A\beta_{1-40}$ is added to $A\beta_{1-40}$, the kinetics are weakly affected, mirroring the fact that, above 20 µM in $A\beta_{1-40}$, $^{ox}A\beta_{1-40}$ has little impact on $A\beta_{1-40}$ aggregation. One main difference appears when comparing the results at equimolar ratio (10:10 µM and 20:20 µM, Figures 4B and 5A). Strikingly, adding 10 µM of $^{ox}A\beta_{1-40}$ has a deep slowdown effect on

$A\beta_{1–40}$, but not at 20 µM. This indicates that 20 µM (or a concentration in between 10 and 20 µM) represents a threshold value above which $^{ox}A\beta_{1–40}$ is not able to significantly interfere with $A\beta_{1–40}$ assembly.

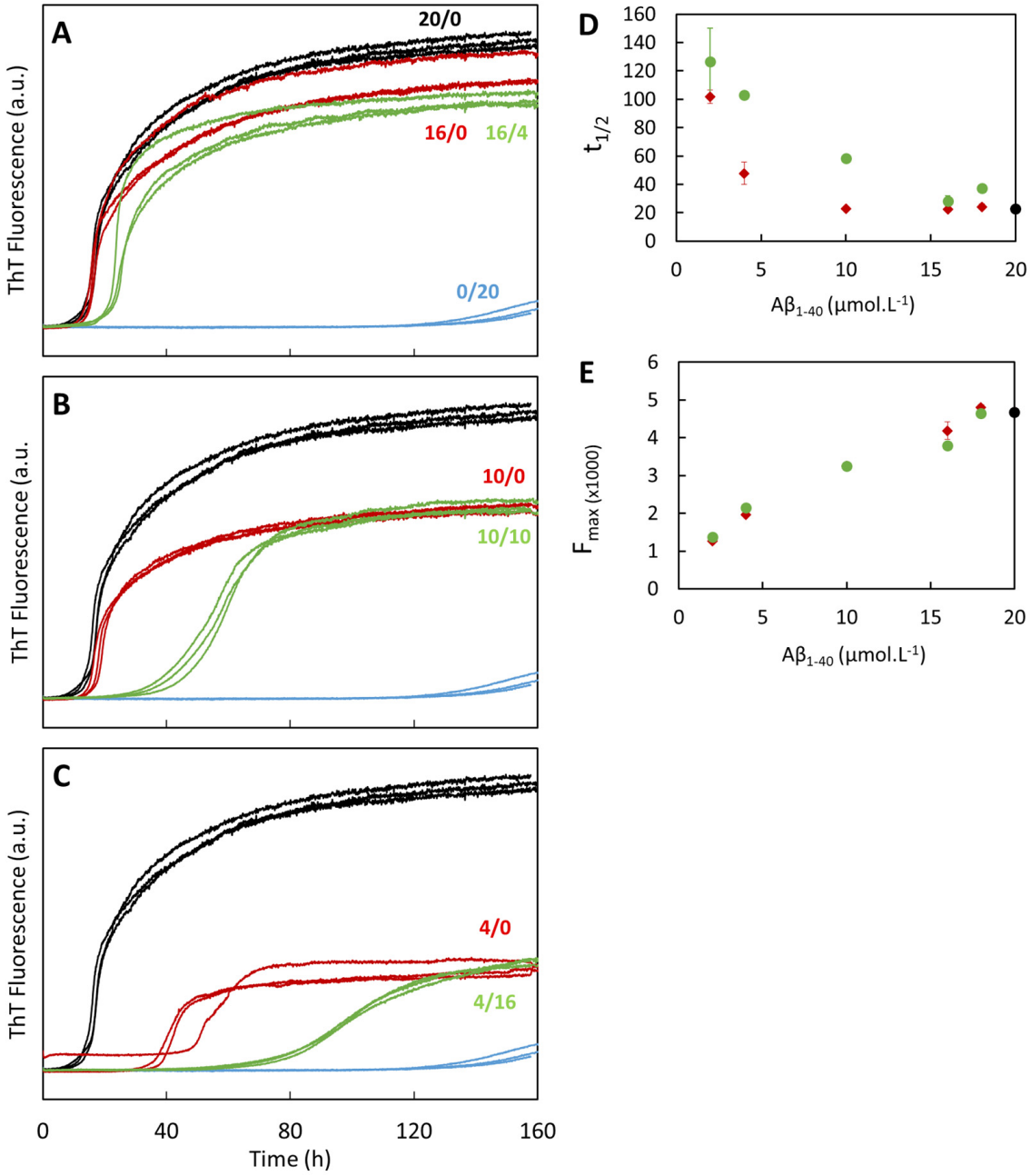

Figure 4. Kinetic monitoring of $A\beta_{1–40}$ and $^{ox}A\beta_{1–40}$ co-assembly using ThT fluorescence as a function of the ratio between peptides (Experiment N°1). Curves are shown as triplicate. $[A\beta_{1–40}]/[^{ox}A\beta_{1–40}]$ = 20/0 µM (black), 0/20 µM (blue), 16/4 µM (green), 16/0 µM (red) (**A**); $[A\beta_{1–40}]/[^{ox}A\beta_{1–40}]$ = 10/10 µM (green), 10/0 µM (red) (**B**); $[A\beta_{1–40}]/[^{ox}A\beta_{1–40}]$ = 4/16 µM (green), 4/0 µM (red) (**C**). Average $t_{1/2}$ (**D**) and F_{max} (**E**) values as a function of the $A\beta_{1–40}$ concentration with $^{ox}A\beta_{1–40}$ presence ($[A\beta_{1–40}]$ + $[^{ox}A\beta_{1–40}]$ = 20 µM) (green dots) or without (red dots). HEPES buffer 50 mM, [NaCl] = 65 mM, pH 7.4. Y-axis corresponds in panel A–C to ThT fluorescence in arbitrary unit (a.u.); data are directly comparable between them (same y-scale).

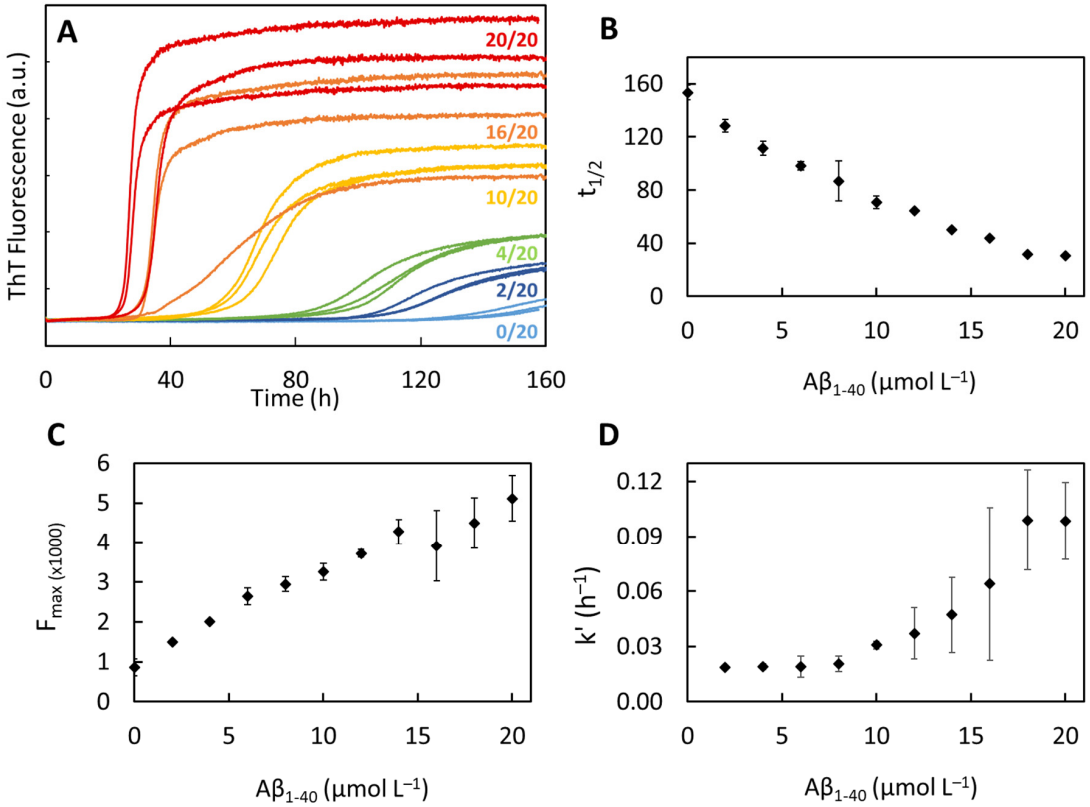

Figure 5. Kinetic monitoring of $A\beta_{1–40}$ and $^{ox}A\beta_{1–40}$ co-assembly using ThT fluorescence as a function of addition of $A\beta_{1–40}$ to $[A\beta_{1–40}]$ = 20 µM. Curves are shown as triplicate. All curves $[^{ox}A\beta_{1–40}]$ = 20 µM + $[A\beta_{1–40}]$ = 0 µM (blue), 2 µM (dark blue), 4 µM (green), 10 µM (yellow), 16 µM (orange), 20 µM (red) (**A**). From experiment N°1: HEPES buffer 50 mM, [NaCl] = 65 mM, pH 7.4. Y-axis corresponds to ThT fluorescence in arbitrary unit (a.u.); data are directly comparable between them (same y-scale). (**B**–**D**) Average $t_{1/2}$, F_{max} and k' values as a function of the $[A\beta_{1–40}]$ with $^{ox}A\beta_{1–40}$ present ($[^{ox}A\beta_{1–40}]$ = 20 µM). Data from curves of Figure 5 and Figure S7.

3.5. Impact of Cu(II) and Zn(II) on the Self-Assembly of $A\beta_{1–40}$ and $^{ox}A\beta_{1–40}$ and Their Co-Assembly

- *Self-assembly of $A\beta_{1–40}$:* In the presence of 0.9 equiv. of Cu(II), the $A\beta_{1–40}$ assembly splits into two processes. It starts very rapidly, with a no-lag phase, and reaches a weak fluorescence plateau (approximately 5-fold weaker than the plateau value of apo-$A\beta_{1–40}$ assembly); then, a second sigmoidal process occurs after about 30 h, leading to a final plateau intensity approximately two times lower than the one observed for apo-$A\beta_{1–40}$ (Figure 6 and Figure S10, left, solid and dashed black lines). TEM pictures illustrate the presence of deposits of fibrils that are shorter and thinner than those of the apo-$A\beta_{1–40}$ (Figure 7A, Figures S11A and S12A). A similar kinetic behavior is observed in the presence of 0.9 equiv. Zn(II) (Figure 6 and Figure S10, right, solid and dashed black lines), but with a much higher fluorescence intensity. Fibrils are mostly detected by TEM at the end of aggregation, in line with the high plateau intensity (Figure 7C, Figures S11C and S12C). In contrast to the apo-$A\beta_{1–40}$ fibrils, the Zn-$A\beta_{1–40}$ fibrils are untangled and thinner, but form clumps. In presence of either cations, the kinetics of fibrils formation show a quite unusual profile with two distinct phases. We may hypothesize that the first fast-forming aggregates are further reorganized in more stable fibrillar species during the second phase. Note that this two-step trend was observed on all the independent experiments.
- *Self-assembly of $^{ox}A\beta_{1–40}$:* In the presence of 0.9 equiv. of Cu(II), the ThT fluorescence curve of $^{ox}A\beta_{1–40}$ shows a very weak intensity that appears after a rapid increase (Figure 6, left, blue solid line and inset). No sigmoidal process is observed at the

time scale of the experiment in contrast to Cu-A$\beta_{1–40}$ aggregation (Figure 6, black line). Although the final plateau of ThT fluorescence intensity is very low, the TEM pictures show the presence of oligomeric species and amorphous aggregates, along with some fibrils of various morphologies (Figure 7B, Figures S11B and S12B). In line with the observation made for the apo peptides, their formation may be triggered by the presence of the remaining A$\beta_{1–40}$ in the sample. The apparent divergence between ThT fluorescence and TEM results may also originate from the formation of fibrils (i) having weak interaction with ThT, (ii) having interaction with ThT but giving rise to a low fluorescence enhancement or (iii) with the quenching of the ThT fluorescence by the Cu(II) paramagnetism, since the Cu(II) site is altered by the oxidation of the peptide [70]. In the presence of 0.9 equiv. Zn(II), the ThT fluorescence intensity rapidly reaches its maximal value, which is quite weak compared to Zn-A$\beta_{1–40}$ (about 5-times lower). In line with the lower fluorescence plateau value, less fibrils are observed by TEM, where dense deposits of amorphous aggregates are also present (Figure 7D, Figures S11D and S12D).

- *Co-assembly:* Furthermore, we also studied the assembly behavior of an equimolar mixture of A$\beta_{1–40}$ and ^{ox}A$\beta_{1–40}$ in the presence of 0.9 equiv. of Cu(II) or Zn(II) (Figure 6, solid green lines). With Cu(II), the two-step kinetics is recovered, with a first plateau value weaker than the one for Cu-A$\beta_{1–40}$, and a second sigmoidal process that takes more time to occur (about 60 h versus 20 h). This is reminiscent of what was previously reported in the case of the self-assembly of Cu_2-A$\beta_{1–40}$ (in the presence of 2 Cu(II) ion per A$\beta_{1–40}$ peptide), and suggests that Cu(II) is weakly bound to ^{ox}A$\beta_{1–40}$ (at least weaker than the second site in A$\beta_{1–40}$) and that it can mainly be transferred to A$\beta_{1–40}$ [21]. The formation of ternary ^{ox}A$\beta_{1–40}$-Cu-A$\beta_{1–40}$ is also possible. With Zn(II), the kinetic trace is half-way from that of Zn-A$\beta_{1–40}$ and Zn-^{ox}A$\beta_{1–40}$, in line with various possible events at play (independent assembly of Zn-A$\beta_{1–40}$ and Zn-^{ox}A$\beta_{1–40}$, or the assembly of Zn_2-A$\beta_{1–40}$), prevents deeper analysis.

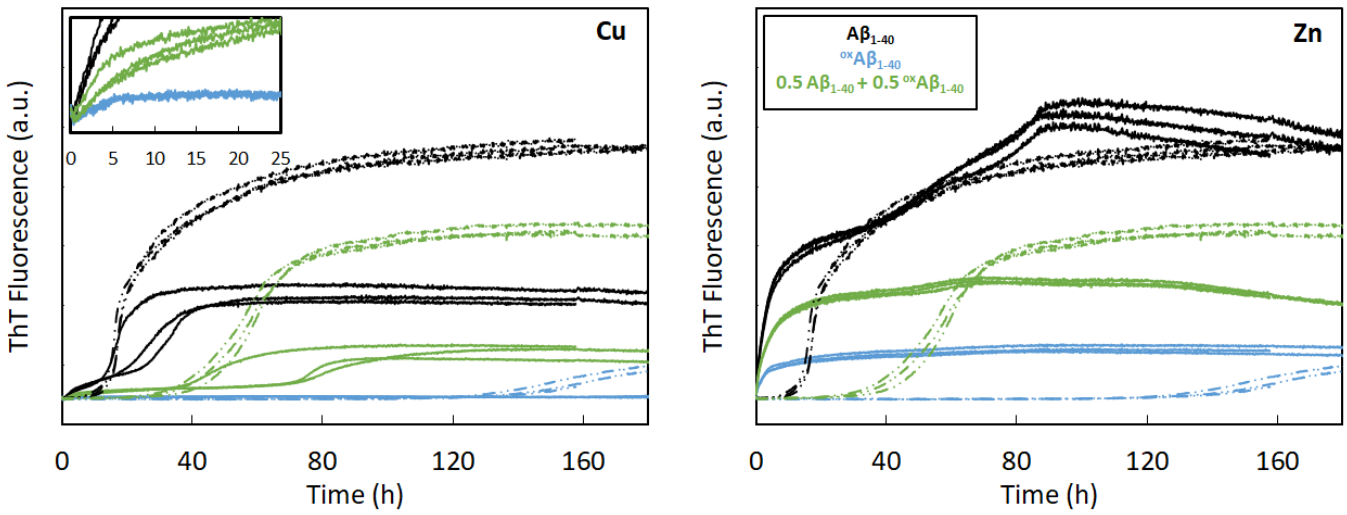

Figure 6. Kinetic monitoring of A$\beta_{1–40}$ and ^{ox}A$\beta_{1–40}$ co-assembly in presence of Cu(II) or Zn(II) using ThT fluorescence. Curves are shown as triplicate. [A$\beta_{1–40}$] = 20 µM (black); [A$\beta_{1–40}$] = [^{ox}A$\beta_{1–40}$] = 10 µM (green); [^{ox}A$\beta_{1–40}$] = 20 µM (blue). Apo peptides (dashed curves) with Cu(II) (18 µM, solid curves, left panel) or Zn(II) (18 µM, solid curves, right panel) at pH 7.4. Data from Experiment N°1: HEPES buffer 50 mM, NaCl 65 mM. Y-axis corresponds to ThT fluorescence in arbitrary unit (a.u.); data are directly comparable between them (same y-scale).

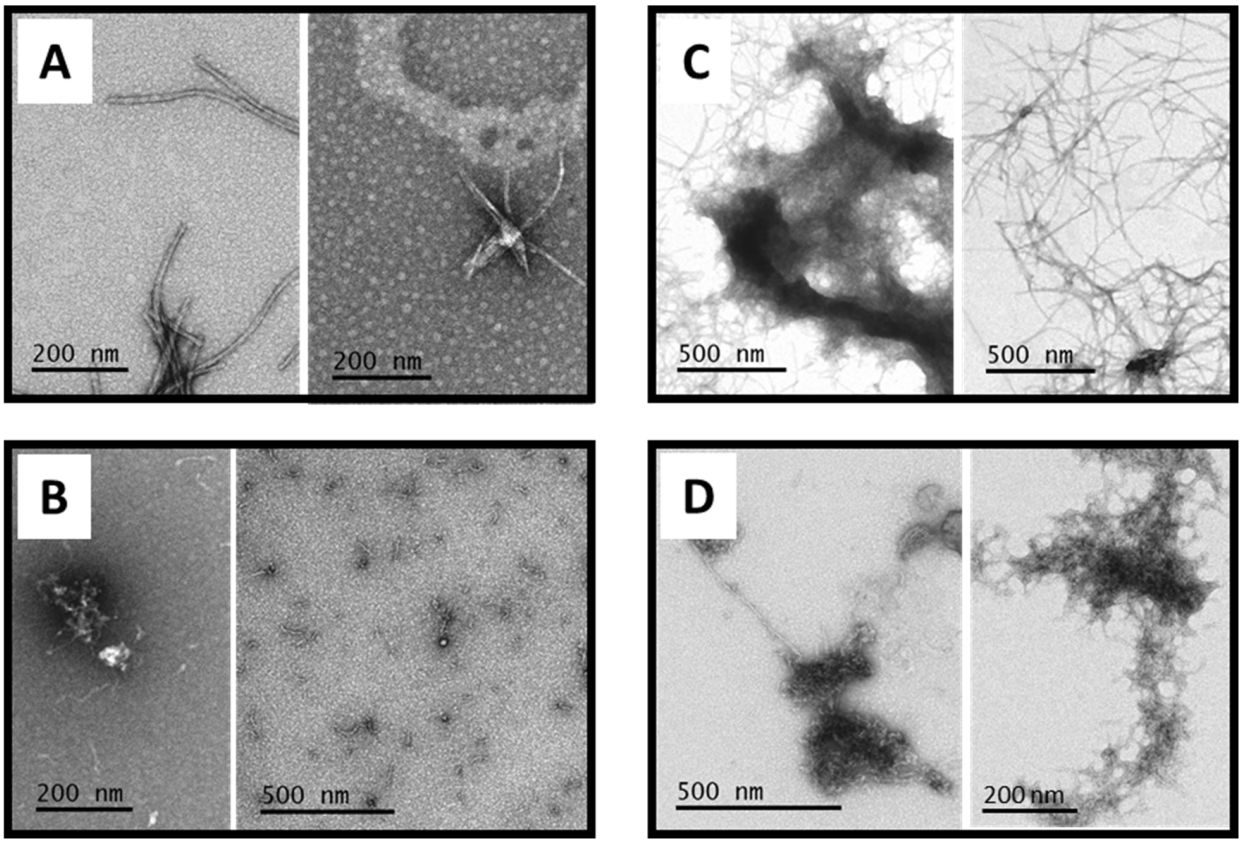

Figure 7. Selected TEM pictures of Cu($A\beta_{1-40}$) and Cu($^{ox}A\beta_{1-40}$) at 20 µM ((**A**) and (**B**), respectively) and of Zn($A\beta_{1-40}$) and Zn($^{ox}A\beta_{1-40}$) at 20 µM ((**C**) and (**D**), respectively) taken at the end of the ThT fluorescence experiment N°1. Hepes buffer 50 mM, [NaCl] = 65 mM, pH 7.4. Two shots are given to better illustrate the heterogeneity of the assemblies formed.

4. Concluding Remarks

4.1. Reproducibility Issues

We acknowledge that batch effects are the first cause of non-reproducible data in amyloid kinetics assessments in vitro [12,79]. However, the converging results from our various datasets emphasize that the assembly trends and their response to multiple stimuli (pH, metal ions, ratio of peptides in their mixture . . .) discussed in this work are consistent. Furthermore, the trends observed in the presence of $^{ox}A\beta_{1-40}$ are known to be dependent on the level of oxidation that can fluctuate between experiments. Hence, it is quite remarkable that, despite these two sources of variability, the trends we observed in both the kinetics and amyloids morphology point toward the same conclusions.

4.2. Ability of $^{ox}A\beta_{1-40}$ to Self-Assemble and Importance of the Oxidation Paths of $A\beta_{1-40}$

The present study shows that the oxidative damages undergone by $A\beta_{1-40}$ during the ROS production, catalyzed by the Cu-$A\beta_{1-40}$, in the presence of ascorbate as reductant and dioxygen, have a strong impact on the assembly processes. To our knowledge, there is no report on $^{ox}A\beta_{1-40}$ with multiple oxidation sites mirroring the biological complexity, including oxidation on the His to form the 2-oxo-His. Indeed, in contrast to the previous studies, $^{ox}A\beta_{1-40}$ refers to a set of oxidized $A\beta_{1-40}$ species, which includes oxidative modifications mainly on Asp1, His13 and His14 in our experimental conditions [35], and which are more biologically relevant than the site-specific oxidative modifications studied before [36–44]. This difference in the oxidation process participates in some divergent data, with respect to the literature [63–69], whilst the previous trend of a slow-down of the assembly, induced by oxidation, is also obtained here. The $^{ox}A\beta_{1-40}$ species keep

their ability to aggregate, but at a much lower rate, and generate amorphous and smaller assemblies rather than long and thick β-sheet rich fibrils, usually observed with non-oxidized $A\beta_{1–40}$. In a very recent paper [20], Tian and Viles found that the pKa values (about 6.7) of the three His residues [82,83] of $A\beta_{1–40}$, rather than the pI (5.3), play a substantial role in the modification of the kinetic assembly trends, with disruption of the electrostatic interactions due to protonated His residues, leading to weaker primary nucleation. In the context of $^{ox}A\beta_{1–40}$, 2-oxo-His are neutral and are formed from pH well beyond 6.7 [84]. Hence, this may explain the lower self-assembly propensity of $^{ox}A\beta_{1–40}$ compared to $A\beta_{1–40}$. In the presence of Cu(II) or Zn(II) ion, the extent of $^{ox}A\beta_{1–40}$ assembly is also much weaker than that of $A\beta_{1–40}$.

4.3. Effect of $^{ox}A\beta_{1–40}$ on $A\beta_{1–40}$ Assembly

The oxidation of the peptide has a strong impact on its assembly (Scheme 3), as shown in both our kinetic and morphology assessments. We demonstrated the fact that, despite a range of 10–40% of non-oxidized $A\beta_{1–40}$ peptide remaining in $^{ox}A\beta_{1–40}$ samples, $^{ox}A\beta_{1–40}$ was able to delay the $A\beta_{1–40}$ assembly that is not driven by a dilution effect. Given this, we demonstrated a modulatory activity of the $^{ox}A\beta_{1–40}$ peptides towards the assembly of $A\beta_{1–40}$: a delaying effect with a reduction of the $t_{1/2}$ and an increase in the growth rate. Interestingly, this delaying effect is partially observed in the presence of Cu(II) (on the second sigmoidal step), but not in the presence of Zn(II), suggesting that the reorganization towards more fibrillary architectures is hampered by the formation of the amorphous $^{ox}A\beta_{1–40}$-Zn species.

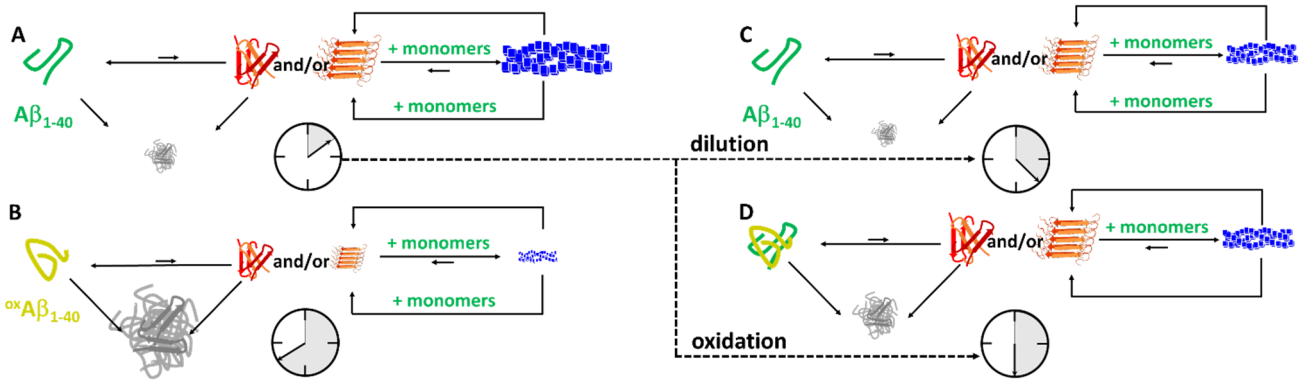

Scheme 3. Proposed summary of the assembly processes under focus. Comparison between $A\beta_{1–40}$ (**A**) and $^{ox}A\beta_{1–40}$ (**B**) (both at 20 μM), and between $A\beta_{1–40}$ ((**C**), $[A\beta_{1–40}]$ = 10 μM) and a mixture of $A\beta_{1–40}$ and $^{ox}A\beta_{1–40}$ ((**D**), $[A\beta_{1–40}] = [^{ox}A\beta_{1–40}]$ = 10 μM). Size of the various aggregation species mirrors the contribution of the various morphology, as detected by TEM and the clocks, and the kinetic of fibrils formation, as probed by ThT fluorescence.

4.4. Effect of pH

We found that $^{ox}A\beta_{1–40}$ delays the $A\beta_{1–40}$ assembly in a wide range of pH (6.0–7.4), while a strong pH dependence of $^{ox}A\beta_{1–40}$ assembly is observed, id est, there is a much slower self-assembly at pH 7.4 compared to pH 6.0, induced by deprotonation of remaining non-oxidized His residues or N-terminal amine. This may be explained by the disruption of electrostatic interactions [21], as reported for related amyloid-forming peptides [20] and for peptides approaching global neutrality with decreasing pH [85].

4.5. Mechanistic Insights

Here, we suggest a tentative mechanism, taking into account our findings, illustrated in Scheme 3. On the left side, the self-assembly of $A\beta_{1–40}$ and $^{ox}A\beta_{1–40}$ are compared. Upon oxidation, the peptide loses most of its ability to form ThT-responsive fibrils (lower level of β-sheet rich fibrils, in blue) and their formation takes a longer time (clock), while the

formation of ill-defined intermediate size species is observed (higher level of off-pathways assemblies, in grey). On the right side, the co-assembly of $A\beta_{1-40}$ and $^{ox}A\beta_{1-40}$ (both at 10 μM) is compared to the self-assembly of $A\beta_{1-40}$ at 10 μM. The same levels of fibrils are formed, but their formation takes longer in the presence of $^{ox}A\beta_{1-40}$ (clock), while the level of off-pathways is higher.

Further mechanistic investigations to gain more insights into the role of Cu(II) and Zn(II) include a pH-dependent study of the effect of the metal ions on the assembly and co-assembly of $A\beta_{1-40}$ and $^{ox}A\beta_{1-40}$, which is currently under progress in our lab.

4.6. Biological Relevance

The results shown here are in line with recent reports showing the impact of Aβ oxidation on aggregation [43,86], although the authors mainly focused on the effect of Met35 oxidation [65,67,87] and emphasized the intricacy of the connection between the different aggregation effectors studied here (Aβ oxidation and metal ions). One general trend is the observation of more heterogeneous and smaller size aggregates with the $^{ox}A\beta_{1-40}$ peptide, leading to weaker ThT fluorescence, including in the presence of metal ions. This might have fallouts with respect to the toxicity of Aβ-based aggregates, since it is now quite well-accepted that oligomers are more toxic than mature fibrils [47,88].

With respect to the biological relevance, further work could include the study of the impact of Fe(II) on the assembly and co-assembly of $A\beta_{1-40}$ and $^{ox}A\beta_{1-40}$ to complement Cu(II) and Zn(II) studied here.

Supplementary Materials: The following supporting information can be downloaded at: https://www.mdpi.com/article/10.3390/antiox12020472/s1, Figure S1: Full mass spectrum of DAEFR and its oxidation products obtained by high-resolution mass spectrometry; Figure S2: Mass spectrometry analysis of $^{ox}A\beta_{1-40}$; Figure S3: Kinetic monitoring of $A\beta_{1-40}$ and $^{ox}A\beta_{1-40}$ co-assembly as a function of pH; Figures S4 and S5: Selected TEM pictures of $A\beta_{1-40}$ and $^{ox}A\beta_{1-40}$; Figure S6: Kinetic monitoring of $A\beta_{1-40}$ and $^{ox}A\beta_{1-40}$ co-assembly as a function of ratio between peptides; Figures S7 and S8: Kinetic monitoring of $A\beta_{1-40}$ and $^{ox}A\beta_{1-40}$ co-assembly as a function of addition of $A\beta_{1-40}$ to $^{ox}A\beta_{1-40}$; Figure S9: Kinetic monitoring of $A\beta_{1-40}$ and $^{ox}A\beta_{1-40}$ co-assembly as a function of addition of $^{ox}A\beta_{1-40}$ to $A\beta_{1-40}$; Figure S10: Kinetic monitoring of $A\beta_{1-40}$ and $^{ox}A\beta_{1-40}$ co-assembly in presence of Cu(II) or Zn(II); Figures S11 and S12: Selected TEM pictures of Cu($A\beta_{1-40}$) and Cu($^{ox}A\beta_{1-40}$) and of Zn($A\beta_{1-40}$) and Zn($^{ox}A\beta_{1-40}$).

Author Contributions: Conceptualization, C.H., F.C. and C.C.; methodology, C.C.; validation, C.H., F.C. and C.C.; formal analysis, C.H. and C.C.; investigation, C.C.; data curation, C.C., L.S. and C.H.; writing—original draft preparation, C.H., F.C. and C.C.; writing—review and editing, C.H., F.C. and C.C.; visualization, C.H., F.C., C.C. and L.S.; supervision, C.H., F.C. and C.C. All authors have read and agreed to the published version of the manuscript.

Funding: ERC StG aLzINK (638712) and ANR AlzABox (ANR 13 BSV5 0016 01).

Institutional Review Board Statement: Not applicable.

Informed Consent Statement: Not applicable.

Data Availability Statement: Data is contained within the article and Supplementary Material.

Acknowledgments: C.H., F.C., L.S. and C.C. acknowledge ERC StG aLzINK (638712, allocated to C.H.) and ANR AlzABox (ANR 13 BSV5 0016 01, allocated to F.C.) for financial support and Peter Faller for fruitful discussions. C.H. thanks Jonathan Pansieri for relevant comments and improvements on the revised manuscript.

Conflicts of Interest: The authors declare no conflict of interest.

References

1. Chatani, E.; Yuzu, K.; Ohhashi, Y.; Goto, Y. Current Understanding of the Structure, Stability and Dynamic Properties of Amyloid Fibrils. *Int. J. Mol. Sci.* **2021**, *22*, 4349. [CrossRef] [PubMed]
2. Almeida, Z.L.; Brito, R.M.M. Structure and Aggregation Mechanisms in Amyloids. *Molecules* **2020**, *25*, 1195. [CrossRef]

3. Willbold, D.; Strodel, B.; Schröder, G.F.; Hoyer, W.; Heise, H. Amyloid-type Protein Aggregation and Prion-like Properties of Amyloids. *Chem. Rev.* **2021**, *121*, 8285–8307. [CrossRef]
4. Iadanza, M.G.; Jackson, M.P.; Hewitt, E.W.; Ranson, N.A.; Radford, S.E. A new era for understanding amyloid structures and disease. *Nat. Rev. Mol. Cell Biol.* **2018**, *19*, 755–773. [CrossRef] [PubMed]
5. Ke, P.C.; Zhou, R.; Serpell, L.C.; Riek, R.; Knowles, T.P.J.; Lashuel, H.A.; Gazit, E.; Hamley, I.W.; Davis, T.P.; Fändrich, M.; et al. Half a century of amyloids: Past, present and future. *Chem. Soc. Rev.* **2020**, *49*, 5473–5509. [CrossRef]
6. Selkoe, D.J.; Hardy, J. The amyloid hypothesis of Alzheimer's disease at 25 years. *EMBO Mol. Med.* **2016**, *8*, 595–608. [CrossRef]
7. Hureau, C. Chapter 7 Role of Metal Ions in Alzheimer's Disease: Mechanistic Aspects Contributing to Neurotoxicity. In *Alzheimer's Disease: Recent Findings in Pathophysiology, Diagnostic and Therapeutic Modalities*; Govindaraju, T., Ed.; The Royal Society of Chemistry: London, UK, 2022; pp. 170–192.
8. Hampel, H.; Hardy, J.; Blennow, K.; Chen, C.; Perry, G.; Kim, S.H.; Villemagne, V.L.; Aisen, P.; Vendruscolo, M.; Iwatsubo, T.; et al. The Amyloid-β Pathway in Alzheimer's Disease. *Mol. Psychiatry* **2021**, *26*, 5481–5503. [CrossRef]
9. Lane, C.A.; Hardy, J.; Schott, J.M. Alzheimer's disease. *Eur. J. Neurol.* **2018**, *25*, 59–70. [CrossRef]
10. Kametani, F.; Hasegawa, M. Reconsideration of Amyloid Hypothesis and Tau Hypothesis in Alzheimer's Disease. *Front. Neurosci.* **2018**, *12*, 25. [CrossRef]
11. Naseri, N.N.; Wang, H.; Guo, J.; Sharma, M.; Luo, W. The complexity of tau in Alzheimer's disease. *Neurosci. Lett.* **2019**, *705*, 183–194. [CrossRef] [PubMed]
12. Faller, P.; Hureau, C. Reproducibility Problems of Amyloid-β Self-Assembly and How to Deal With Them. *Front. Chem.* **2021**, *8*, 611227. [CrossRef] [PubMed]
13. Sinnige, T. Molecular mechanisms of amyloid formation in living systems. *Chem. Sci.* **2022**, *13*, 7080–7097. [CrossRef] [PubMed]
14. Buell, A.K. The growth of amyloid fibrils: Rates and mechanisms. *Biochem. J.* **2019**, *476*, 2677–2703. [CrossRef]
15. Törnquist, M.; Michaels, T.C.T.; Sanagavarapu, K.; Yang, X.; Meisl, G.; Cohen, S.I.A.; Knowles, T.P.J.; Linse, S. Secondary nucleation in amyloid formation. *Chem. Commun.* **2018**, *54*, 8667–8684. [CrossRef]
16. Karamanos, T.K.; Kalverda, A.P.; Thompson, G.S.; Radford, S.E. Mechanisms of amyloid formation revealed by solution NMR. *Prog. Nucl. Magn. Reson. Spectrosc.* **2015**, *88–89*, 86–104. [CrossRef] [PubMed]
17. Meisl, G.; Kirkegaard, J.B.; Arosio, P.; Michaels, T.C.; Vendruscolo, M.; Dobson, C.M.; Linse, S.; Knowles, T.P. Molecular mechanisms of protein aggregation from global fitting of kinetic models. *Nat. Protoc.* **2016**, *11*, 252–272. [CrossRef]
18. Hadi Alijanvand, S.; Peduzzo, A.; Buell, A.K. Secondary Nucleation and the Conservation of Structural Characteristics of Amyloid Fibril Strains. *Front. Mol. Biosci.* **2021**, *8*, 669994. [CrossRef]
19. Linse, S. Monomer-dependent secondary nucleation in amyloid formation. *Biophys. Rev.* **2017**, *9*, 329–338. [CrossRef] [PubMed]
20. Tian, Y.; Viles, J.H. pH Dependence of Amyloid-β Fibril Assembly Kinetics: Unravelling the Microscopic Molecular Processes. *Angew. Chem. Int. Ed. Engl.* **2022**, *61*, e202210675. [CrossRef] [PubMed]
21. Stefaniak, E.; Atrian-Blasco, E.; Goch, W.; Sabater, L.; Hureau, C.; Bal, W. The aggregation pattern of Aβ1-40 is altered by the presence of N-truncated Aβ4-40 and/or Cu(II) ions in a similar way via ionic interactions. *Chemistry* **2021**, *27*, 2798–2809. [CrossRef]
22. Viles, J.H.; Barritt, J.D.; Younan, N.D. N-Terminally Truncated Amyloid-β(11-40/42) Co-Fibrillises with its Full-Length Counterpart, Implications for Alzheimer's Disease. *Angew. Chem. Int. Ed.* **2017**, *56*, 9816–9819. [CrossRef]
23. Cukalevski, R.; Yang, X.; Meisl, G.; Weininger, U.; Bernfur, K.; Frohm, B.; Knowles, T.P.J.; Linse, S. The Aβ40 and Aβ42 peptides self-assemble into separate homomolecular fibrils in binary mixtures but cross-react during primary nucleation. *Chem. Sci.* **2015**, *6*, 4215–4233. [CrossRef] [PubMed]
24. Weiffert, T.; Meisl, G.; Flagmeier, P.; De, S.; Dunning, C.J.R.; Frohm, B.; Zetterberg, H.; Blennow, K.; Portelius, E.; Klenerman, D.; et al. Increased Secondary Nucleation Underlies Accelerated Aggregation of the Four-Residue N-Terminally Truncated Aβ42 Species Aβ5–42. *ACS Chem. Neurosci.* **2019**, *10*, 2374–2384. [CrossRef] [PubMed]
25. Liang, R.; Tian, Y.; Viles, J.H. Cross-seeding of WT amyloid-β with Arctic but not Italian familial mutants accelerates fibril formation in Alzheimer's disease. *J. Biol. Chem.* **2022**, *298*, 102071. [CrossRef] [PubMed]
26. Quartey, M.O.; Nyarko, J.N.K.; Maley, J.M.; Barnes, J.R.; Bolanos, M.A.C.; Heistad, R.M.; Knudsen, K.J.; Pennington, P.R.; Buttigieg, J.; De Carvalho, C.E.; et al. The Aβ(1–38) peptide is a negative regulator of the Aβ(1–42) peptide implicated in Alzheimer disease progression. *Sci. Rep.* **2021**, *11*, 431. [CrossRef]
27. Yano, Y.; Takeno, A.; Matsuzaki, K. Trace amounts of pyroglutaminated Aβ-(3–42) enhance aggregation of Aβ-(1–42) on neuronal membranes at physiological concentrations: FCS analysis of cell surface. *Biochim. Biophys. Acta Biomembr.* **2018**, *1860*, 1603–1608. [CrossRef]
28. Heo, C.E.; Choi, T.S.; Kim, H.I. Competitive homo- and hetero- self-assembly of amyloid-β 1–42 and 1–40 in the early stage of fibrillation. *Int. J. Mass Spectrom.* **2018**, *428*, 15–21. [CrossRef]
29. Cheignon, C.; Tomas, M.; Bonnefont-Rousselot, D.; Faller, P.; Hureau, C.; Collin, F. Oxidative stress and the amyloid beta peptide in Alzheimer's Disease. *Redox Biol.* **2018**, *14*, 450–464. [CrossRef]
30. Atrian-Blasco, E.; Gonzalez, P.; Santoro, A.; Alies, B.; Faller, P.; Hureau, C. Cu and Zn coordination to amyloid peptides: From fascinating chemistry to debated pathological relevance. *Coord. Chem. Rev.* **2018**, *375*, 38–55. [CrossRef]
31. Cheignon, C.; Collin, F.; Faller, P.; Hureau, C. Is ascorbate Dr Jekyll or Mr Hyde in the Cu(Aβ) mediated oxidative stress linked to Alzheimer's Disease? *Dalton Trans.* **2016**, *45*, 12627–12631. [CrossRef] [PubMed]

32. Harrison, F.E.; May, J.M. Vitamin C function in the brain: Vital role of the ascorbate transporter SVCT2. *Free Radic. Biol. Med.* **2009**, *46*, 719–730. [CrossRef]
33. Rice, M.E. Ascorbate regulation and its neuroprotective role in the brain. *Trends Neurosci.* **2000**, *23*, 209–216. [CrossRef]
34. Cassagnes, L.-E.; Hervé, V.; Nepveu, F.; Hureau, C.; Faller, P.; Collin, F. The catalytically active copper-amyloid-Beta state: Coordination site responsible for reactive oxygen species production. *Angew. Chem. Int. Ed.* **2013**, *52*, 11110–11113. [CrossRef] [PubMed]
35. Cheignon, C.; Hureau, C.; Collin, F. Real-time evolution of Aβ40 metal-catalyzed oxidation reveals Asp1 as the main target and a dependence on metal binding site. *Inorganica Chim. Acta* **2018**, *472*, 111–118. [CrossRef]
36. Kowalik-Jankowska, T.; Ruta, M.; Wiśniewska, K.; Łankiewicz, L.; Dyba, M. Products of Cu(II)-catalyzed oxidation in the presence of hydrogen peroxide of the 1–10, 1–16 fragments of human and mouse β-amyloid peptide. *J. Inorg. Biochem.* **2004**, *98*, 940–950. [CrossRef]
37. Inoue, K.; Nakagawa, A.; Hino, T.; Oka, H. Screening Assay for Metal-Catalyzed Oxidation Inhibitors Using Liquid Chromatography−Mass Spectrometry with an N-Terminal β-Amyloid Peptide. *Anal. Chem.* **2009**, *81*, 1819–1825. [CrossRef]
38. Pirota, V.; Dell'Acqua, S.; Monzani, E.; Nicolis, S.; Casella, L. Copper-Aβ Peptides and Oxidation of Catecholic Substrates: Reactivity and Endogenous Peptide Damage. *Chem. Eur. J.* **2016**, *22*, 16964–16973. [CrossRef]
39. Nadal, R.C.; Rigby, S.E.J.; Viles, J.H. Amyloid β−Cu2+ Complexes in both Monomeric and Fibrillar Forms Do Not Generate H2O2 Catalytically but Quench Hydroxyl Radicals. *Biochemistry* **2008**, *47*, 11653–11664. [CrossRef]
40. Inoue, K.; Garner, C.; Ackermann, B.L.; Oe, T.; Blair, I.A. Liquid chromatography/tandem mass spectrometry characterization of oxidized amyloid beta peptides as potential biomarkers of Alzheimer's disease. *Rapid Commun. Mass Spectrom.* **2006**, *20*, 911–918. [CrossRef] [PubMed]
41. Schöneich, C.; Williams, T.D. Cu(II)-Catalyzed Oxidation of β-Amyloid Peptide Targets His13 and His14 over His6: Detection of 2-Oxo-histidine by HPLC-MS/MS. *Chem. Res. Toxicol.* **2002**, *15*, 717–722. [CrossRef] [PubMed]
42. Atwood, C.S.; Perry, G.; Zeng, H.; Kato, Y.; Jones, W.D.; Ling, K.-Q.; Huang, X.; Moir, R.D.; Wang, D.; Sayre, L.M.; et al. Copper Mediates Dityrosine Cross-Linking of Alzheimer's Amyloid-β. *Biochemistry* **2004**, *43*, 560–568. [CrossRef] [PubMed]
43. Gu, M.; Bode, D.C.; Viles, J.H. Copper Redox Cycling Inhibits Aβ Fibre Formation and Promotes Fibre Fragmentation, while Generating a Dityrosine Aβ Dimer. *Sci. Rep.* **2018**, *8*, 16190. [CrossRef] [PubMed]
44. Vázquez, G.; Caballero, A.B.; Kokinda, J.; Hijano, A.; Sabaté, R.; Gamez, P. Copper, dityrosine cross-links and amyloid-β aggregation. *J. Biol. Inorg. Chem.* **2019**, *24*, 1217–1229. [CrossRef]
45. Houée-Lévin, C.; Bobrowski, K.; Horakova, L.; Karademir, B.; Schöneich, C.; Davies, M.J.; Spickett, C.M. Exploring oxidative modifications of tyrosine: An update on mechanisms of formation, advances in analysis and biological consequences. *Free Radic. Res.* **2015**, *49*, 347–373. [CrossRef]
46. Atrian-Blasco, E.; Conte-Daban, A.; Hureau, C. Mutual interference of Cu and Zn ions in Alzheimer's disease: Perspectives at the molecular level. *Dalton Trans.* **2017**, *46*, 12750–12759. [CrossRef]
47. Rana, M.; Sharma, A.K. Cu and Zn interactions with Ab peptides: Consequence of coordination on aggregation and formation of neurotoxic soluble Ab oligomers. *Metallomics* **2019**, *11*, 64–84. [CrossRef]
48. Han, J.; Du, Z.; Lim, M.H. Mechanistic Insight into the Design of Chemical Tools to Control Multiple Pathogenic Features in Alzheimer's Disease. *Acc. Chem. Res.* **2021**, *54*, 3930–3940. [CrossRef] [PubMed]
49. Chen, L.-L.; Fan, Y.-G.; Zhao, L.-X.; Zhang, Q.; Wang, Z.-Y. The metal ion hypothesis of Alzheimer's disease and the anti-neuroinflammatory effect of metal chelators. *Bioorganic Chem.* **2023**, *131*, 106301. [CrossRef]
50. Wang, T.; Xu, S.-F.; Fan, Y.-G.; Li, L.-B.; Guo, C. Iron Pathophysiology in Alzheimer's Diseases. In *Brain Iron Metabolism and CNS Diseases*; Chang, Y.-Z., Ed.; Springer: Singapore, 2019; pp. 67–104.
51. Yang, L.; Nao, J. Ferroptosis: A potential therapeutic target for Alzheimer's disease. *Rev. Neurosci.* **2022**. [CrossRef]
52. Bousejra-ElGarah, F.; Bijani, C.; Coppel, Y.; Faller, P.; Hureau, C. Iron(II) binding to amyloid-beta, the Alzheimer's peptide. *Inorg. Chem.* **2011**, *50*, 9024–9030. [CrossRef] [PubMed]
53. Nair, N.G.; Perry, G.; Smith, M.A.; Reddy, V.P. NMR Studies of Zinc, Copper, and Iron Binding to Histidine, the Principal Metal Ion Complexing Site of Amyloid-β Peptide. *J. Alzheimer's Dis.* **2010**, *20*, 57–66. [CrossRef]
54. Pal, A.; Cerchiaro, G.; Rani, I.; Ventriglia, M.; Rongioletti, M.; Longobardi, A.; Squitti, R. Iron in Alzheimer’s Disease: From Physiology to Disease Disabilities. *Biomolecules* **2022**, *12*, 1248. [CrossRef] [PubMed]
55. Tran, D.; DiGiacomo, P.; Born, D.E.; Georgiadis, M.; Zeineh, M. Iron and Alzheimer's Disease: From Pathology to Imaging. *Front. Hum. Neurosci.* **2022**, *16*, 838692. [CrossRef] [PubMed]
56. Chen, W.-T.; Liao, Y.-H.; Yu, H.-M.; Cheng, I.H.; Chen, Y.-R. Distinct Effects of Zn2+, Cu2+, Fe3+, and Al3+ on Amyloid-β Stability, Oligomerization, and Aggregation: Amyloid-β Destabilization Promotes Annular Protofibril Formation. *J. Biol. Chem.* **2011**, *286*, 9646–9656. [CrossRef]
57. Everett, J.; Céspedes, E.; Shelford, L.R.; Exley, C.; Collingwood, J.F.; Dobson, J.; van der Laan, G.; Jenkins, C.A.; Arenholz, E.; Telling, N.D. Ferrous iron formation following the co-aggregation of ferric iron and the Alzheimer's disease peptide β-amyloid (1–42). *J. R. Soc. Interface* **2014**, *11*, 20140165. [CrossRef]
58. Liu, B.; Moloney, A.; Meehan, S.; Morris, K.; Thomas, S.E.; Serpell, L.C.; Hider, R.; Marciniak, S.J.; Lomas, D.A.; Crowther, D.C. Iron Promotes the Toxicity of Amyloid β-Peptide by Impeding Its Ordered Aggregation. *J. Biol. Chem.* **2011**, *286*, 4248–4256. [CrossRef]

59. Tahmasebinia, F.; Emadi, S. Effect of metal chelators on the aggregation of beta-amyloid peptides in the presence of copper and iron. *BioMetals* **2017**, *30*, 285–293. [CrossRef] [PubMed]
60. Everett, J.; Brooks, J.; Lermyte, F.; O'Connor, P.B.; Sadler, P.J.; Dobson, J.; Collingwood, J.F.; Telling, N.D. Iron stored in ferritin is chemically reduced in the presence of aggregating Aβ(1-42). *Sci. Rep.* **2020**, *10*, 10332. [CrossRef]
61. Pedersen, J.T.; Chen, S.W.; Borg, C.B.; Ness, S.; Bahl, J.M.; Heegaard, N.H.; Dobson, C.M.; Hemmingsen, L.; Cremades, N.; Teilum, K. Amyloid-β and α-Synuclein Decrease the Level of Metal-Catalyzed Reactive Oxygen Species by Radical Scavenging and Redox Silencing. *J. Am. Chem. Soc.* **2016**, *138*, 3966–3969. [CrossRef]
62. Jiang, D.; Li, X.; Liu, L.; Yagnik, G.B.; Zhou, F. Reaction Rates and Mechanism of the Ascorbic Acid Oxidation by Molecular Oxygen Facilitated by Cu(II)-Containing Amyloid-β Complexes and Aggregates. *J. Phys. Chem. B* **2010**, *114*, 4896–4903. [CrossRef]
63. Razzokov, J.; Yusupov, M.; Bogaerts, A. Oxidation destabilizes toxic amyloid beta peptide aggregation. *Sci. Rep.* **2019**, *9*, 5476. [CrossRef]
64. Li, K.S.; Rempel, D.L.; Gross, M.L. Conformational-Sensitive Fast Photochemical Oxidation of Proteins and Mass Spectrometry Characterize Amyloid Beta 1–42 Aggregation. *J. Am. Chem. Soc.* **2016**, *138*, 12090–12098. [CrossRef] [PubMed]
65. Friedemann, M.; Helk, E.; Tiiman, A.; Zovo, K.; Palumaa, P.; Tõugu, V. Effect of methionine-35 oxidation on the aggregation of amyloid-β peptide. *Biochem. Biophys. Rep.* **2015**, *3*, 94–99. [CrossRef] [PubMed]
66. Palmblad, M.; Westlind-Danielsson, A.; Bergquist, J. Oxidation of Methionine 35 Attenuates Formation of Amyloid β-Peptide 1-40 Oligomers. *J. Biol. Chem.* **2002**, *277*, 19506–19510. [CrossRef]
67. Gu, M.; Viles, J.H. Methionine oxidation reduces lag-times for amyloid-β(1–40) fiber formation but generates highly fragmented fibers. *Biochim. Biophys. Acta Proteins Proteom* **2016**, *1864*, 1260–1269. [CrossRef]
68. Pilkington, A.W.T.; Donohoe, G.C.; Akhmedov, N.G.; Ferrebee, T.; Valentine, S.J.; Legleiter, J. Hydrogen Peroxide Modifies Aβ-Membrane Interactions with Implications for Aβ(40) Aggregation. *Biochemistry* **2019**, *58*, 2893–2905. [CrossRef] [PubMed]
69. O'Malley, T.T.; Witbold, W.M.; Linse, S.; Walsh, D.M. The Aggregation Paths and Products of Aβ42 Dimers Are Distinct from Those of the Aβ42 Monomer. *Biochemistry* **2016**, *55*, 6150–6161. [CrossRef]
70. Cheignon, C.; Faller, P.; Testemale, D.; Hureau, C.; Collin, F. Metal-catalyzed oxidation of Aβ and the resulting reorganization of Cu binding sites promote ROS production. *Metallomics* **2016**, *8*, 1081–1089. [CrossRef]
71. Atrian-Blasco, E.; Del Barrio, M.; Faller, P.; Hureau, C. Ascorbate Oxidation by Cu(Amyloid-β) Complexes: Determination of the Intrinsic Rate as a Function of Alterations in the Peptide Sequence Revealing Key Residues for Reactive Oxygen Species Production. *Anal. Chem.* **2018**, *90*, 5909–5915. [CrossRef]
72. Walsh, D.M.; Selkoe, D.J. Amyloid β-protein and beyond: The path forward in Alzheimer's disease. *Curr. Opin. Neurobiol.* **2020**, *61*, 116–124. [CrossRef]
73. Collin, F.; Cheignon, C.; Hureau, C. Oxidative stress as a biomarker for Alzheimer's Disease. *Biomark. Med.* **2018**, *12*, 201–203. [CrossRef]
74. Wärmländer, S.K.T.S.; Österlund, N.; Wallin, C.; Wu, J.; Luo, J.; Tiiman, A.; Jarvet, J.; Gräslund, A. Metal binding to the amyloid-β peptides in the presence of biomembranes: Potential mechanisms of cell toxicity. *J. Biol. Inorg. Chem.* **2019**, *24*, 1189–1196. [CrossRef]
75. LeVine, H. Quantification of β-sheet amyloid fibril structures with thioflavin T. *Methods Enzymol.* **1999**, *309*, 274–284. [CrossRef] [PubMed]
76. Reinke, A.A.; Gestwicki, J.E. Insight into amyloid structure using chemical probes. *Chem. Biol. Drug Des.* **2011**, *77*, 399–411. [CrossRef] [PubMed]
77. Noël, S.; Cadet, S.; Gras, E.; Hureau, C. The benzazole scaffold: A SWAT to combat Alzheimer's Disease. *Chem. Soc. Rev.* **2013**, *42*, 7747–7762. [CrossRef] [PubMed]
78. Gade Malmos, K.; Blancas-Mejia, L.M.; Weber, B.; Buchner, J.; Ramirez-Alvarado, M.; Naiki, H.; Otzen, D. ThT 101: A primer on the use of thioflavin T to investigate amyloid formation. *Amyloid* **2017**, *24*, 1–16. [CrossRef]
79. Martins, P.M.; Navarro, S.; Silva, A.; Pinto, M.F.; Sárkány, Z.; Figueiredo, F.; Pereira, P.J.B.; Pinheiro, F.; Bednarikova, Z.; Burdukiewicz, M.; et al. MIRRAGGE—Minimum Information Required for Reproducible AGGregation Experiments. *Front. Neurosci.* **2020**, *13*, 582488. [CrossRef]
80. Shoffner, S.K.; Schnell, S. Estimation of the lag time in a subsequent monomer addition model for fibril elongation. *Phys. Chem. Chem. Phys.* **2016**, *18*, 21259–21268. [CrossRef]
81. Bentea, L.; Watzky, M.A.; Finke, R.G. Sigmoidal Nucleation and Growth Curves Across Nature Fit by the Finke–Watzky Model of Slow Continuous Nucleation and Autocatalytic Growth: Explicit Formulas for the Lag and Growth Times Plus Other Key Insights. *J. Phys. Chem. C* **2017**, *121*, 5302–5312. [CrossRef]
82. Kowalik-Jankowska, T.; Ruta, M.; Wisniewska, K.; Lankiewicz, L. Coordination abilities of the 1-16 and 1-28 fragments of b-amyloid peptide towards copper(II) ions: A combined potentiometric and spectroscopic study. *J. Inorg. Biochem.* **2003**, *95*, 270–282. [CrossRef]
83. Hureau, C.; Coppel, Y.; Dorlet, P.; Solari, P.L.; Sayen, S.; Guillon, E.; Sabater, L.; Faller, P. Deprotonation of the Asp1-Ala2 Peptide Bond Induces Modification of the Dynamic Copper(II) Environment in the Amyloid-b Peptide near Physiological pH. *Angew. Chem. Int. Ed.* **2009**, *48*, 9522–9525. [CrossRef] [PubMed]
84. Garrett, H.M. A Study into the Influence of Amyloid-beta Peptide Oxidation on the Rate of Fibril Formation, with a Synthesis of 2-oxo-Histidine. Ph.D. Thesis, Queen Mary University of London, London, UK, 2012.

85. Alies, B.; La Penna, G.; Sayen, S.; Guillon, E.; Hureau, C.; Faller, P. Insights into the Mechanisms of Amyloid Formation of ZnII-Ab11-28: pH-Dependent Zinc Coordination and Overall Charge as Key Parameters for Kinetics and the Structure of ZnII-Ab11-28 Aggregates. *Inorg. Chem.* **2012**, *51*, 7897–7902. [CrossRef] [PubMed]
86. Kang, J.; Lee, S.J.C.; Nam, J.S.; Lee, H.J.; Kang, M.-G.; Korshavn, K.J.; Kim, H.-T.; Cho, J.; Ramamoorthy, A.; Rhee, H.-W.; et al. An Iridium(III) Complex as a Photoactivatable Tool for Oxidation of Amyloidogenic Peptides with Subsequent Modulation of Peptide Aggregation. *Chem. Eur. J.* **2017**, *23*, 1645–1653. [CrossRef] [PubMed]
87. Hou, L.; Lee, H.G.; Han, F.; Tedesco, J.M.; Perry, G.; Smith, M.A.; Zagorski, M.G. Modification of amyloid-β1-42 fibril structure by methionine-35 oxidation. *J. Alzheimer's Dis.* **2013**, *37*, 9–18. [CrossRef] [PubMed]
88. Lee, S.J.C.; Nam, E.; Lee, H.J.; Savelieff, M.G.; Lim, M.H. Towards an understanding of amyloid-β oligomers: Characterization, toxicity mechanisms, and inhibitors. *Chem. Soc. Rev.* **2017**, *46*, 310–323. [CrossRef] [PubMed]